

Ray-tracing based analysis of channel  
characteristics and capacity improvement  
capabilities of spatial multiplexing and  
beamforming at 15 and 28 GHz

Qingbi Liao  
wir14qli@student.lu.se

Department of Electrical and Information Technology  
Lund University

Examiner: Fredrik Rusek

Advisor: Carl Gustafson, Zhinong Ying

October 20, 2016



---

## Acknowledgements

---

I would like to express sincere gratitude towards my supervisors, Carl Gustafson and Zhinong Ying, for giving me the chance of conducting the study about mm-Wave. Their professional advises have guided me out of a quandary so many times, and those advises are also the encouragement I needed for later studies. They have spent so much time on answering my questions and are so patient that explanations are always in detailed as much as possible.

In addition, the indoor channel and material permittivity measurements are carried out by Carl Gustafson, which are the very important foundation of this work. Without his support, this project can not be conducted further. Besides, the patch and monopole antennae of 15 and 28 GHz and their patterns are provided by Zhinong Ying, which extends this work out of the limit of the isotropic antenna case. Based on that, the comparison between the indoor simulation and the measurement is possible, the key point in this project.

I would really appreciate the support from Peter Karlsson, whose professional experience of mm-Wave and insight comments help this project proceed smoothly. My thanks to Thomas Bolin, Erik Lennart Bengtsson, and Kun Zhao of Sony Mobile Communications. They have taken part in the meetings of this work and given me significant opinions and suggestions. Special thanks to Fredrik Harrysson from Ericsson for his help about the knowledge of the outdoor measurement system. Also I am grateful for the kindness and friendliness of all members in the Network Technology department during my stay at Sony.



---

## Abstract

---

In the previous decades, mm-Wave frequency bands have largely been ignored for cellular communication because of the high free space attenuation as well as the cost and complexity of mm-Wave RF circuits. However, with the improvement of RF and antenna technologies over the last decade, it has become feasible to consider mm-Wave bands for cellular communications. With the large bandwidths available in the mm-Wave range, this could enable much higher data rates, and could also alleviate the problem of limited frequency resources. Many bands in the frequency range above 6 GHz and into the mm-Wave range of 30-300 GHz are therefore interesting candidates for future 5G cellular systems. The utilisation of *Multiple-input Multiple-output* (MIMO) is almost a necessity at these frequencies. This makes it possible to implement different antenna processing techniques in order to improve coverage and system capacity. In the master thesis, the behaviour of 15 and 28 GHz channels in indoor and outdoor scenarios are simulated by using a ray-tracing algorithm. By comparing indoor channel measurements with the ray-tracing results, it is possible to verify the performance and identify the limitations of the ray-tracing algorithm. In the outdoor scenario, channel characteristics such as received power and RMS delay spreads are analysed based on ray-tracing simulations. A metric called *Channel Multiplexing Richness* (CMR) is defined to indicate the scattering richness of a location. This thesis also investigates the capacity improving capabilities of beamforming (such as directional beamforming and dominant eigenmode transmission), spatial multiplexing and a hybrid technique which combines beamforming and spatial multiplexing. The link capacity for these different techniques is calculated based on ray tracing results for the single-user case, assuming full channel state information. The simulation results are also compared to different environment models, so that the influences of the material permittivity and the level of geometric details are investigated.



---

# Table of Contents

---

<b>1</b>	<b>Introduction</b>	<b>1</b>
1.1	Background . . . . .	2
1.2	Overall aim . . . . .	3
1.3	Concrete goals . . . . .	3
1.4	Outline . . . . .	3
<b>2</b>	<b>Theory</b>	<b>5</b>
2.1	MIMO channel characteristics . . . . .	5
2.2	Antenna processing techniques . . . . .	8
2.3	Ray-tracing algorithm . . . . .	12
<b>3</b>	<b>Methology</b>	<b>13</b>
3.1	Synthesised antenna pattern . . . . .	13
3.2	Indoor scenario properties . . . . .	17
3.3	Indoor measurement . . . . .	21
3.4	Outdoor scenario properties . . . . .	22
<b>4</b>	<b>Indoor measurement and simulation comparison</b>	<b>27</b>
4.1	Indoor 15 GHz $1 \times 100$ MISO PDP and received power . . . . .	29
4.2	Indoor 28 GHz $49 \times 49$ MIMO PDP . . . . .	33
<b>5</b>	<b>Outdoor scenario channel characteristics</b>	<b>35</b>
5.1	Channel multiplexing richness . . . . .	35
5.2	Simulating $1 \times 32$ MISO received power . . . . .	38
5.3	RMS delay spread of $8 \times 32$ MIMO channel with isotropic element . . . . .	41
<b>6</b>	<b>Outdoor <math>8 \times 32</math> MIMO channel Capacity</b>	<b>45</b>
6.1	Capacity distribution and CDF comparison . . . . .	45
6.2	Capacity of rotating receiver . . . . .	51
<b>7</b>	<b>Conclusion</b>	<b>55</b>
7.1	Future work . . . . .	55
	<b>References</b>	<b>57</b>

<b>A</b>	<b>Appendix</b>	<b>61</b>
A.1	Indoor scenario . . . . .	61
A.2	Outdoor scenario . . . . .	67



---

## List of Figures

---

2.1	A $2 \times 2$ MIMO spatial multiplexing system. . . . .	10
2.2	Two antenna elements case of HB2. . . . .	11
2.3	Radio waves transmission, reflection, and diffraction; $A(x_1, y_1, z_1)$ diffraction point, $B(x_1, y_1, z_1)$ reflection point. . . . .	12
3.1	Synthesising the virtual antenna array by the first element of the simulated array. . . . .	14
3.2	The PDP comparison of the simulated antenna array and synthesised antenna array. . . . .	16
3.3	Replacing the isotropic antenna pattern with the patch antenna pattern. . . . .	17
3.4	Patch antenna pattern. . . . .	18
3.5	Monopole antenna pattern of 15 GHz . . . . .	19
3.6	Indoor 15 GHz detailed three-dimensional model in the ray-tracer . . . . .	20
3.7	Indoor 15 GHz two-dimensional sky view in the ray-tracer . . . . .	21
3.8	Indoor 15 GHz simplified three-dimensional model . . . . .	22
3.9	Outdoor real environment Kistagangen, Kista, Stockholm. . . . .	23
3.10	Outdoor virtual model sky view in the ray-tracer. . . . .	24
3.11	Outdoor three-dimensional detailed car model in the ray-tracer . . . . .	24
3.12	Outdoor 15 GHz simplified model with concrete building blocks . . . . .	25
3.13	Outdoor MIMO antenna array structure . . . . .	26
4.1	Indoor 15 GHz channel multiplexing richness . . . . .	28
4.2	Indoor simplified model channel multiplexing richness . . . . .	28
4.3	Indoor 28 GHz channel multiplexing richness . . . . .	29
4.4	Indoor 15 GHz PDP Rx1 comparison of the measurement and two simulation models . . . . .	30
4.5	Indoor 15 GHz AOD Rx1 . . . . .	32
4.6	Indoor 28 GHz PDP comparison . . . . .	33
5.1	Outdoor 15 GHz SISO isotropic antenna element CMR distribution . . . . .	35
5.2	Outdoor 15 GHz <i>Simple concrete model</i> CMR distribution . . . . .	36
5.3	Outdoor 15 GHz <i>Simple model</i> CMR distribution . . . . .	37
5.4	Outdoor 28 GHz SISO isotropic antenna element CMR distribution . . . . .	38
5.5	Outdoor 15 GHz MISO DET received power . . . . .	39

5.6	Outdoor 15 GHz received power corner loss comparison among three different models . . . . .	40
5.7	Outdoor 15 GHz MISO DET received power by distance comparison among three different models . . . . .	41
5.8	Outdoor 28 GHz MISO DET received power . . . . .	42
5.9	Outdoor 15 and 28 GHz MISO DET received power by distance comparison . . . . .	42
5.10	Outdoor 15 and 28 GHz MISO DET received power CDF comparison . . . . .	43
5.11	Outdoor MIMO system isotropic antenna element delay spread with distance . . . . .	43
5.12	Outdoor MIMO system patch antenna element delay spread distribution . . . . .	44
6.1	Outdoor 15 GHz spatial multiplexing capacity distribution . . . . .	47
6.2	Outdoor 15 GHz spatial multiplexing capacity CDF comparison . . . . .	48
6.3	Outdoor 28 GHz spatial multiplexing capacity distribution . . . . .	49
6.4	Outdoor 28 GHz spatial multiplexing capacity CDF comparison . . . . .	50
6.5	Outdoor receiver positions of varying orientations . . . . .	51
6.6	Outdoor 15 GHz Rx19 rotating capacity . . . . .	53
6.7	Outdoor 15 GHz Rx19 rotating capacity CDF and angular spread . . . . .	54
A.1	Indoor 15 GHz MISO PDP comparison Rx1 . . . . .	61
A.2	Indoor 15 GHz MISO PDP comparison Rx1 magnified . . . . .	62
A.3	Indoor 15 GHz MISO PDP comparison Rx2 . . . . .	62
A.4	Indoor 15 GHz MISO PDP comparison Rx2 magnified . . . . .	63
A.5	Indoor 15 GHz MISO PDP comparison Rx3 . . . . .	63
A.6	Indoor 15 GHz MISO PDP comparison Rx3 magnified . . . . .	64
A.7	Indoor 15 GHz MISO PDP comparison Rx4 . . . . .	64
A.8	Indoor 15 GHz MISO PDP comparison Rx4 magnified . . . . .	65
A.9	Indoor 15 GHz AOD Rx2 view from transmitter . . . . .	65
A.10	Indoor 15 GHz AOD Rx2 angular spread with delay time . . . . .	66
A.11	Indoor 15 GHz AOD Rx3 view from transmitter . . . . .	66
A.12	Indoor 15 GHz AOD Rx3 angular spread with delay time . . . . .	67
A.14	Outdoor 15 GHz isotropic BF capacity . . . . .	67
A.13	Outdoor 15 GHz isotropic DET capacity . . . . .	68
A.17	Outdoor 15 GHz patch DET capacity . . . . .	68
A.15	Outdoor 15 GHz isotropic SMH2 capacity . . . . .	69
A.16	Outdoor 15 GHz isotropic SMH4 capacity . . . . .	69
A.18	Outdoor 15 GHz patch BF capacity . . . . .	70
A.19	Outdoor 15 GHz patch SMH2 capacity . . . . .	70
A.20	Outdoor 15 GHz patch SMH4 capacity . . . . .	71
A.21	Outdoor 28 GHz isotropic DET capacity . . . . .	71
A.22	Outdoor 28 GHz isotropic BF capacity . . . . .	72
A.23	Outdoor 28 GHz isotropic SMH2 capacity . . . . .	72
A.24	Outdoor 28 GHz isotropic SMH4 capacity . . . . .	73
A.25	Outdoor 28 GHz patch DET capacity . . . . .	73
A.26	Outdoor 28 GHz patch BF capacity . . . . .	74
A.27	Outdoor 28 GHz patch SMH2 capacity . . . . .	74

A.28 Outdoor 28 GHz patch SMH4 capacity . . . . .	75
A.29 Outdoor 15 GHz rotating capacity of Rx44 . . . . .	76
A.30 Outdoor 15 GHz Rx44 rotating capacity CDF and angular spread . .	77
A.31 Outdoor 15 GHz rotating capacity of Rx82 . . . . .	78
A.32 Outdoor 15 GHz Rx82 rotating capacity CDF and angular spread . .	79
A.33 Outdoor 28 GHz rotating capacity of Rx19 . . . . .	80
A.34 Outdoor 28 GHz Rx19 rotating capacity CDF and angular spread . .	81
A.35 Outdoor 28 GHz rotating capacity of Rx44 . . . . .	82
A.36 Outdoor 28 GHz Rx44 rotating capacity CDF and angular spread . .	83
A.37 Outdoor 28 GHz rotating capacity of Rx82 . . . . .	84
A.38 Outdoor 28 GHz Rx82 rotating capacity CDF and angular spread . .	85



---

## List of Tables

---

3.1	Indoor communication system of 15 and 28 GHz . . . . .	17
3.2	Indoor material measured permittivities . . . . .	19
3.3	Indoor parameters in ray-tracer . . . . .	20
3.4	Outdoor detailed car model material permittivity and conductivity . .	26
4.1	Indoor 15 GHz MISO DET received power comparison . . . . .	29
4.2	Indoor 15 GHz MISO received power Rx1 . . . . .	30
6.1	Outdoor street route area 10% outage capacity [bps/Hz] . . . . .	45



# Introduction

---

The next generation of cellular system, also known as 5G, is currently being standardised for future communication system with higher requirements. Since traditional communication systems, such as LTE and WIFI, are limited to certain frequency bands, in 5G, the investigation moves forward to the promising *Super High Frequency band* (SHF), from 3 to 30 GHz and *Extremely High Frequency band* (EHF) from 30 to 300 GHz [1]. In [2], the possibility of using the millimeter wave for communication has been verified, which inspires more and more studies focused on bands above 6 GHz. One of the main challenges of communicating using mm-Waves is the high free space loss. The mm-Wave frequency band provides an enormous amount of available spectrum which includes local multipoint service at 28 to 30 GHz and free-licensed 60 GHz band [3]. This research focuses on the 15 and 28 GHz frequency bands.

In [3], six key factors of enabling mm-Wave communication is mentioned. The two most important elements are the knowledge of channel characteristics and the utilisation of spatial processing techniques. At these higher frequency bands, a smaller wavelength of radio waves in millimeter scale makes it possible to construct complex antenna arrays; more antennae can be implemented within the same size area comparing to low frequency antenna arrays [4]. This way, a large number of antennas can be employed at both the base station and the user equipment on a small area. This enables improved array processing techniques, such as beamforming and spatial multiplexing. The spatial multiplexing and beamforming are two common antenna processing techniques used in the communication system to combat the increased path loss and also to improve the channel capacity. This work investigated the channel performance of utilising the spatial multiplexing and beamforming techniques at 15 and 28 GHz based on both measurement data and simulation results. The simulation is built on a ray-tracing-based software called *Wireless Insite*. The comparison between the measurement results and simulation data shows the feasibility of managing a ray-tracing method to analyse the channel situation. Based on that, more simulation models are assessed to explore the communication characteristics in realistic environments. Their differences are compared to work out the impact of factors, such as material permittivity and level of details of virtual scenarios, on simulation results.

## 1.1 Background

Research around 28 GHz, focusing on channel characteristics are mostly based on measurements, which usually takes a long time. In [5], the channel path loss properties at 28 GHz of two large indoor spots, railway station and airport terminal, is studied in both *Line-of-sight* (LOS) and *Non-line-of-sight* (NLOS) environments. Besides path loss, paper [6] analyses RMS delay spread, *Power Angle Profile* (PAP) and *Power Delay Profile* (PDP) of the indoor scenario based on measurement data collected by *Vector Network Analyser* (VNA). The outdoor channel propagation characteristics at 28 GHz is measured in [7]. Recently, the indoor channel propagation at 23.5 and 45 GHz have been compared through ray-tracing and VNA measured methods in [8]. However, most of the papers focus on only one of these two aspects, either measurement or ray-tracing simulation. Few studies have compared channel properties based on the simulation data and measurement data. Also, 15 GHz is a typical and interesting frequency band at EHF. There is not many studies carried out around this frequency band. In [9], the path loss and human body shadowing loss from 6 to 30 GHz is being investigated; the path loss result was observed based on the measurement and ray-tracing simulation. At 15 GHz, the channel correlation measurement has been analysed in [10]. The knowledge of channel communication performance at 15 GHz is an essential part of understanding the channel characteristics at EHF. Detailed channel properties at this frequency band remain unknown. Further studies of channel characteristics around 15 GHz are needed to improve the channel knowledge at EHF.

The ray-tracing algorithm is a method which calculates the radio wave propagation paths. In [11], the channel capacity of an indoor MIMO system at 2.4 GHz is analysed with ray-tracing. At 28 GHz band, a three-dimensional channel model of an urban scenario is constructed using ray-tracing in [12] to observe the communication performance at mm-Wave bands and it compares simulation results with a measurement-based path loss model, and in [13], the path loss model is investigated by ray-tracing for both LOS and NLOS in urban environments at 28 GHz.

Compared with the *Single-input Single-output* (SISO) channel link, one significant improvement of the MIMO system is the access to different antenna array configurations, which make it available to implement antenna processing techniques, for example the spatial multiplexing and beamforming. In the indoor scenario with LOS component, the spatial multiplexing is an effective method of increasing the spectral efficiency at 60 GHz in [14]. In [15], the channel capacity of 60 GHz with the spatial multiplexing and beamforming utilised has been compared; and the capacity of spatial multiplexing always outperforms the capacity of beamforming. Besides the utilisation of the spatial multiplexing and beamforming at UHF, it is also interesting to analyse their capacity improvement capabilities at SHF. At 15 and 28 GHz frequency bands, however, only few papers focused on the channel capacity comparisons of different antenna processing techniques.



## 1.2 Overall aim

This work aims to verify the feasibility of the ray-tracing simulation of the wireless channel and explore the SU-MIMO channel characteristics, received power, RMS delay spread, capacity, and etc, at 15 and 28 GHz based on the simulation. The possibility of using 15 and 28 GHz in the 5G communication systems is investigated by observing the system coverage and comparing the influences on channel capacity utilising different antenna processing techniques based on the ray-tracing simulation.

## 1.3 Concrete goals

The indoor 15 GHz channel has been measured using a  $1 \times 100$  MISO system in which a  $10 \times 10$  patch array is utilised at the transmitter side and a single monopole at the receiver side. At 28 GHz, the indoor channel is measured using a  $49 \times 49$  MIMO virtual array with monopole antenna element at both sides. For the outdoor scenario, a  $1 \times 32$  MISO system was simulated to compare the received power with the signal strength measured by [16]. In the simulation, the outdoor communication model is an  $8 \times 32$  SU-MIMO system with isotropic or patch antenna element. The following goals are concluded:

- Indoor and outdoor virtual models creation in the ray-tracer;
- Hybrid beamforming antenna configuration of the UE side;
- The synthesis of SU-MIMO communication system in Matlab based on the simulation data.

## 1.4 Outline

This report consists of seven chapters, *Introduction*, *Theory*, *Methodology*, *Conclusion*, and three chapters 4-6 introduce the results. The motivation, background, and concrete goals are already mentioned in the *Introduction* part. The channel model, simulation tools, antenna processing techniques, and communication system parameters are described in *Theory*. In chapter three, *Methodology*, detailed methods, for example, synthesising virtual antenna arrays or implementing simulation environments in the ray-tracer are explained. Chapter 4-6 show significant results of capacity, received power, and etc, and their comparisons. The last chapter is *Conclusion*.



---

Chapter 2  
Theory

---

The MIMO systems considered in this work involves only the single user case. A frequency flat MIMO channel communication system is modelled as:

$$\mathbf{y} = \sqrt{\frac{E_s}{M_T}} \mathbf{H} \mathbf{s} + \mathbf{n} \quad (2.1)$$

where  $\mathbf{H}$  is  $M_R \times M_T$  MIMO channel matrix.  $M_R$ ,  $M_T$  are the number of receiving and transmitting antennae,  $E_s$  is the average energy of one transmitted symbol, so that  $E_s/M_T$  is the transmitting energy of one antenna element. The column vectors  $\mathbf{s}$ ,  $\mathbf{y}$  are the transmitted and received signals, respectively. The AWGN is described as  $\mathbf{n}$ .

## 2.1 MIMO channel characteristics

Metrics for evaluating the performance of a communication system are introduced in this section. The definition of the channel capacity, received power, channel multiplexing richness, and RMS delay spread are explained. The delay spread is calculated without any consideration of antenna processing techniques and with isotropic antenna element applied, so that the influence of the antenna pattern is eliminated. Detailed explanations are introduced in their corresponding sections.

### 2.1.1 Capacity

The channel capacity is an important parameter commonly used in evaluating communication system performance. It indicates the system ability of transferring information. The mathematical capacity model of the AWGN channel was developed by Claude Shannon in [17]. Compared to a SISO system, the usage of multiple antennae improves the channel capacity, especially when assuming perfect CSI at the transmitter side. The general Space-Time channel capacity definition with CSI comes from [18], and it is calculated as:

$$C = \max_{\mathbf{R}_{ss}} \log_2 \det \left( \mathbf{I} + \frac{E_s}{M_T N_0} \mathbf{H} \mathbf{R}_{ss} \mathbf{H}^H \right) \quad \text{bps/Hz.} \quad (2.2)$$

In the equation 2.2, under the condition of perfect CSI, the channel matrix  $\mathbf{H}$  is known by the transmitter and receiver.  $N_0$  is the AWGN power spectral density.

$\mathbf{R}_{ss}$  is the covariance matrix of input signals, and it changes when utilising different antenna processing techniques.

### 2.1.2 Channel multiplexing richness

The *channel multiplexing richness* (CMR) is defined as the number of plane waves radiated from an isotropic antenna with received power over a fixed threshold. It indicates the available transmission paths from all directions which have a fairly strong received power. The richness threshold  $C_{th}$  is defined as 30 dB higher than the noise power level. The noise level is calculated as below:

$$\sigma^2 = kT_0B10^{\frac{NF}{10}}, \quad (2.3)$$

where  $NF$  is the noise figure of the system,  $B$  is the bandwidth.  $T_0$  is the standard noise temperature 290 K, and  $k$  is the Boltzmann constant,  $1.38 \times 10^{-23}$  J/K. Then, the threshold is:

$$C_{th} = \sigma^2 + 30. \quad (2.4)$$

In the ray-tracing simulation, plane waves are shot from a source point and those eventually arrive the receiver are traced; information of a plane wave, such as AOD, phase, electrical field, and etc, is recorded [19]. The number of rays shot from the source point and traced is fixed. Let  $p_i$  denotes the power of the  $i$ th plane wave carrying, the CMR is calculated as:

$$\text{CMR} = \sum_i C_i, \quad (2.5)$$

where  $C_i$  is defined as:

$$C_i = \begin{cases} 1, & \text{if } p_i \geq C_{th} \\ 0, & \text{if } p_i < C_{th} \end{cases}. \quad (2.6)$$

For example, if there are three plane waves whose power is larger than  $C_{th}$ , then CMR is equal to 3.

The CMR calculation is based on the isotropic SISO channel, which means it completely eliminates the effect of antenna pattern and array pattern, but it is only related with the environment itself. The CMR is investigated at indoor and outdoor scenarios simulated by different virtual models, and it is an important parameter indicating the impact of the level of geometric details and the material permittivity on simulation results.

In the simulation, it will be introduced later that the MIMO array is synthesised from isotropic SISO plane waves by applying the phase shift on each antenna element. The plane wave received power of the antenna element generated by the synthesis stays the same with the original data. Therefore, the number of plane waves with power higher than the threshold is the same for all antenna elements. If the CMR definition involves the MIMO array, then the value is the number of plane waves higher than the threshold times the number of antenna element in the two sides, which grows with the increasing of antenna elements used, obviously. The CMR of the isotropic SISO channel, however, directly and only exhibits the scattering richness of the environment. It is also convenient that, when different MIMO arrays are considered, the MIMO channel richness is calculated by multiplying the SISO CMR with the corresponding antenna number.

### 2.1.3 RMS delay spread

In the wideband system, signals can be distorted by multipath components, which is also known as *Intersymbol Interference* (ISI). *Root mean square* (RMS) delay spread  $S_\tau$  can describe delay dispersion in some situations without knowing the exact shape of the PDP [20]. Assuming  $T_s$  is the symbol duration time, an ISI-free channel can be expected if the communication system satisfies  $T_s \ll S_\tau$  [21]. Equation 2.7 shows the definition of RMS delay spread.

$$S_\tau = \sqrt{\frac{\int_{-\infty}^{+\infty} P_h(\tau)\tau^2 d\tau}{P_m} - T_m^2}, \quad (2.7)$$

where  $P_h(\tau)$  is PDP,  $P_m$  is given by

$$P_m = \int_{-\infty}^{+\infty} P_h(\tau) d\tau, \quad (2.8)$$

and  $T_m$  is defined as

$$T_m = \frac{\int_{-\infty}^{+\infty} P_h(\tau)\tau d\tau}{P_m}. \quad (2.9)$$

Due to the effect of the delay spread, wideband signals cannot be simply described as amplitude and phase random processes, but should be presented by a multipath component representation [21]. The RMS delay spread of an  $8 \times 32$  MIMO channel with isotropic antenna elements is observed in the outdoor scenario at 15 and 28 GHz. The connections between RMS delay spread and frequency and transmission distance are investigated.

### 2.1.4 Total received power

The received power of the  $j$ th antenna element is calculated based on the plane waves with phase information [19]:

$$P_{rx,j} = \frac{\lambda^2 \beta}{8\pi\eta_0} \left| \sum_{i=1}^{N_p} [E_{\theta,i} g_\theta(\theta_i, \phi_i) + E_{\phi,i} g_\phi(\theta_i, \phi_i)] \right|^2 \quad (2.10)$$

where  $N_p$  is the number of plane waves and  $i$  is the index,  $(\theta, \phi)$  indicate the direction of arrival [19]:

$$g_\theta(\theta, \phi) = \sqrt{|G_\theta(\theta, \phi)|} e^{j\psi_\theta}, \quad (2.11)$$

where  $G_\theta$  and  $\psi_\theta$  are the antenna gain and phase of  $\theta$  component. The theta and phi component of the electric field is represented by  $E_\theta$  and  $E_\phi$ , and  $\lambda$  is the wavelength. The free space impedance  $\eta_0$  is equal to  $377 \Omega$ . The quantity  $\beta$  is the

frequency spectrum overlap part of transmitted waveform and receiver frequency sensitivity, which is defined in [19]:

$$\beta = \frac{\int_{f_T - B_T/2}^{f_T + B_T/2} S_T(f) S_R(f) df}{\int_{f_T - B_T/2}^{f_T + B_T/2} S_T(f) df}, \quad (2.12)$$

where  $f_T$  stands for the transmitting centre frequency, and  $B_T$  is the bandwidth.  $S_T(f)$  and  $S_R(f)$  are the transmitted and received waveform.

In the MIMO system, the antenna array at the receiver side contains  $M_R$  antenna elements. And the total power is the sum of received power from individual antenna element:

$$P_{tot} = \sum_{j=1}^{M_R} P_{rx,j}. \quad (2.13)$$

In the indoor scenario, the received power of a  $1 \times 100$  MISO channel is compared between the simulation and measurement data at 15 GHz. In the outdoor scenario, a  $1 \times 32$  MISO system with patch at transmitter side and single monopole at receiver side is simulated to compare the received power with the signal strength of the outdoor measurement in [16].

## 2.2 Antenna processing techniques

The multiple antenna system provides sufficient propagation paths, which makes it possible to implement *antenna processing techniques* (APT). Diversity and spatial multiplexing are two common techniques applied in a MIMO system to improve the communication system performance. The diversity scheme ensures the system reliability while the spatial multiplexing improves the capacity. This section explains the basic principles of three APTs, adaptive beamforming, spatial multiplexing and, hybrid beamforming.

### 2.2.1 Adaptive beamforming

The beamforming technique is an important feature of the MIMO system, aiming at improving the communication system reliability. The adaptive beamforming optimises the SNR by adjusting the beamforming weights adequately, instead of radiating in a fixed direction. The channel model can be expressed as in [22]:

$$y = \mathbf{w}_{RX}^H \mathbf{H} \mathbf{w}_{TX} s + \tilde{n}, \quad (2.14)$$

where  $y$  is the output received signal, and  $s$  is the transmitted signal, and  $\tilde{n}$  is equal to  $\mathbf{w}_{RX}^H \mathbf{n}$ ,  $\mathbf{n}$  is the noise column vector of the channel.  $\mathbf{H}$  is the channel transfer function with size  $M_R \times M_T$ . The column vectors  $\mathbf{w}_{TX}$  and  $\mathbf{w}_{RX}$  are the beamforming weights at the transmitter side and the receiver side, correspondingly. Two beamforming methods are considered with brief descriptions below.

### Directional beamforming

The *directional beamforming* (BF) increases the received signal strength by radiating electrical waves at a chosen direction [23]. The method of finding out the optimal direction is given by [24] as equation 2.15 shows:

$$(\hat{\theta}, \hat{\phi}) = \arg \max_{(\hat{\theta}, \hat{\phi})} \left| \sum_{f_k} \frac{\mathbf{w}^H \text{vec}\{\mathbf{H}(f_k)\}}{\|\mathbf{w}\|_F} \exp(-j2\pi f_k \tau_{\text{peak}}) \right|, \quad (2.15)$$

where  $\mathbf{H}(f_k)$  is the channel transfer function of the  $k$ th sub-channel,  $f_k$  is the subcarrier frequency,  $\mathbf{w}$  is the Kronecker product of the beamforming weights  $\mathbf{w}_{\text{TX}}$  and  $\mathbf{w}_{\text{RX}}$ , calculated as  $\mathbf{w} = \mathbf{w}_{\text{TX}} \otimes \mathbf{w}_{\text{RX}}$ , and  $\tau_{\text{peak}}$  is defined as

$$\tau_{\text{peak}} = \arg \max_{\tau} \{P_h(\tau)\}, \quad (2.16)$$

where  $P_h(\tau)$  is the power delay profile [24]. The equivalent channel after beamforming is represented as:

$$\mathbf{H}_{\text{eq}}(f_k) = \frac{\mathbf{w}^H \text{vec}\{\mathbf{H}(f_k)\}}{\|\mathbf{w}\|_F}, \quad (2.17)$$

### Dominant eigenmode beamforming

Besides concentrating energy at the steering direction, another way of implementing beamforming technique is *Dominant Eigenmode Transmission* (DET). The singular value decomposition of channel  $\mathbf{H}$  is as:

$$\mathbf{H} = \mathbf{U}\mathbf{\Sigma}\mathbf{V}^H, \quad (2.18)$$

where  $\mathbf{\Sigma}$  is the matrix of singular values, and its maximum value is represented by  $\sigma_{\text{max}}$ . The matrices  $\mathbf{U}$ ,  $\mathbf{V}$  stand for the group of singular vectors. The SNR is maximised when the beamforming vectors satisfy that  $\mathbf{w}_{\text{RX}}^H \mathbf{H} \mathbf{w}_{\text{TX}} = \sigma_{\text{max}}$ , and this can be realised by choosing  $\mathbf{w}_{\text{RX}}$ ,  $\mathbf{w}_{\text{TX}}$  to be the corresponding singular vectors of the largest singular value  $\sigma_{\text{max}}$  [25]. Derived from the equation 2.14, the DET channel model is described as:

$$y = \sigma_{\text{max}} s + \tilde{n}. \quad (2.19)$$

### 2.2.2 Spatial multiplexing

Comparing with the beamforming technique, the *spatial multiplexing* (SM) improves the system capacity by transmitting multiple data streams in parallel via different propagation paths. Also, the capacity of spatial multiplexing MIMO system increases linearly with the number of transmitting and receiving antenna pairs [21].

Figure 2.1 is a simple spatial multiplexing configuration with two transmitting antennae and two receiving antennae. Blocks  $S/P$  and  $P/S$  are serial parallel conversions.  $s_1$  and  $s_2$  are the data streams which are available to be sent in

parallel, and  $\tilde{s}_1, \tilde{s}_2$  are the received data streams, correspondingly.  $h_{11}, h_{21}, h_{12},$  and  $h_{22}$  are the elements of the channel matrix  $\mathbf{H}$ , which is represented as:

$$\mathbf{H} = \begin{bmatrix} h_{11} & h_{12} \\ h_{21} & h_{22} \end{bmatrix}. \quad (2.20)$$

The system can transmit two data streams in parallel in a scattering rich environment. The channel model conducted from equation 2.1 is:

$$\begin{bmatrix} \tilde{s}_1 \\ \tilde{s}_2 \end{bmatrix} = \sqrt{\frac{E_s}{2}} \begin{bmatrix} h_{11} & h_{12} \\ h_{21} & h_{22} \end{bmatrix} \begin{bmatrix} s_1 \\ s_2 \end{bmatrix} + \begin{bmatrix} n_1 \\ n_2 \end{bmatrix}. \quad (2.21)$$

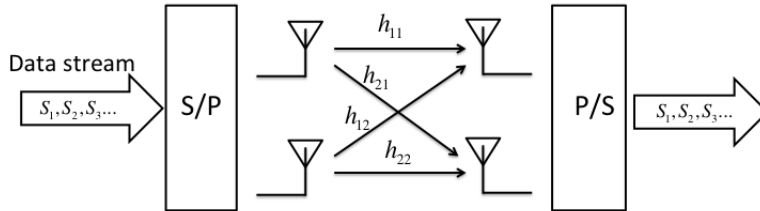


**Figure 2.1:** A  $2 \times 2$  MIMO spatial multiplexing system.

When there is a strong LOS in the channel or only few scattering components exist, the number of data streams that a MIMO system can transmit is smaller than the antenna element number. Assuming  $r$  is the rank of the covariance  $\mathbf{H}\mathbf{H}^H$  of a  $M_R \times M_T$  MIMO channel, the maximum number of data streams available to be transmitted in parallel, also known as degree of freedom, is calculated as:

$$DoF = \min(r, M_T, M_R) \quad (2.22)$$

A full rank channel satisfies that:

$$r = \min(M_T, M_R) \quad (2.23)$$

With the perfect CSI, by applying the *Waterfilling algorithm* [26, 27], it is possible to find out one optimal  $\mathbf{R}_{ss}$  that maximises the MIMO channel capacity. The optimal power allocation of the  $i$ th sub-channel  $\gamma_i^{opt}$  is decided by channel properties and found by the Waterfilling algorithm.  $\lambda_i$  is the corresponding positive eigenvalue of the matrix  $\mathbf{H}\mathbf{H}^H$ . The channel capacity calculation formula is simplified as

$$C = \sum_{i=1}^r \log_2 \left( 1 + \frac{\rho}{M_T} \gamma_i^{opt} \lambda_i \right) \text{ bps/Hz}, \quad (2.24)$$

where  $\rho$  is equal to  $E_s/N_0$  in equation 2.24 and  $r$  is the rank of channel matrix [25].

In the wideband system, capacities of individual subcarriers are different because of the frequency-selective property. To fairly compare the channel capacity of the simulation and measurement results, the frequency band of the wideband



system is divided into  $N$  narrow sub-channel so that each sub-channel is frequency-flat; the capacity of the wideband system is considered as the capacity average among all frequency bins [20] as below:

$$C_{FS} = \frac{1}{N} \sum_{i=1}^N \max_{\mathbf{R}_{ss,i}} \log_2 \det \left( \mathbf{I}_{M_R} + \frac{E_s}{M_T N_0} \mathbf{H}_i \mathbf{R}_{ss,i} \mathbf{H}_i^H \right) \text{ bps/Hz}, \quad (2.25)$$

where  $\mathbf{H}_i$  is the channel matrix of  $i$ th sub-channel,  $\mathbf{R}_{ss,i}$  is the input signal covariance matrix of the  $i$ th sub-channel, correspondingly, and  $\mathbf{I}_{M_R}$  is  $M_R \times M_R$  identity matrix.

### 2.2.3 Hybrid beamforming

The spatial multiplexing is complicated and need the same number of *analog-to-digital* (A/D) or *digital-to-analog* (D/A) converters, which are power consuming components [28]. To simplify the algorithm, a processing technique named as hybrid beamforming which combines the spatial multiplexing and beamforming is utilised. Instead of considering antenna elements completely separated or combined, those elements are divided into small subgroups in the hybrid case, while the antenna array geometry stays the same as full beamforming or spatial multiplexing. Inside each subgroups, the beamforming algorithm is carried out. The spatial multiplexing technique is implemented based on every subgroup.

To achieve the optimal solution, the beamforming weights and spatial multiplexing weights should be considered jointly. However, to simplify the calculation, a suboptimal solution is adopted, which first finds out the beamforming weights of antennae inside a same subgroup, and then applies the spatial multiplexing among subgroups. So that, the number of parallel data streams that a hybrid beamforming system can transmit is related with the number of subgroups.

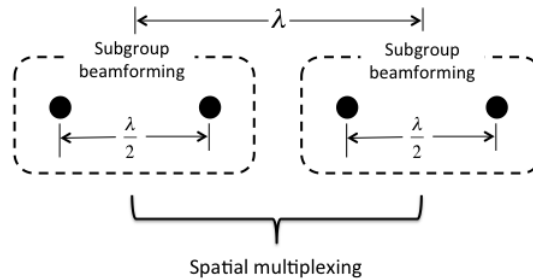


**Figure 2.2:** Two antenna elements case of HB2.

Figure 2.2 is an example of hybrid beamforming configuration with four antenna elements divided into two subgroups. The antenna elements inside a subgroup implement directional beamforming algorithm, and among subgroups spatial multiplexing is implemented. In this work, HB $x$  is the abbreviation of a hybrid beamforming array with subgroups number  $x$ . In this way, figure 2.2 is a four elements linear HB2 array as there are two subgroups.

### 2.3 Ray-tracing algorithm

Ray tracing is a method of high-frequency approximation to Maxwell’s equations complying to Snell’s law, equation 2.26 and following *Geometric optics* (GO) [20].

$$\frac{\sin \theta_1}{\sin \theta_2} = \frac{\lambda_1}{\lambda_2} = \frac{n_2}{n_1}. \quad (2.26)$$

In the equation,  $\theta$  is the angle of the incidence or the refraction;  $\lambda$  is the wavelength and  $n$  is the refraction index. Radio waves propagate from transmitter to receiver mainly in the form of transmission, reflection and diffraction as figure 2.3 shows.  $A(x_1, y_1, z_1)$  is a diffraction point and  $B(x_1, y_1, z_1)$  is a reflection point. In the ray-tracing simulation, radio waves are considered as rays to emulate propagation paths of plane waves [20].

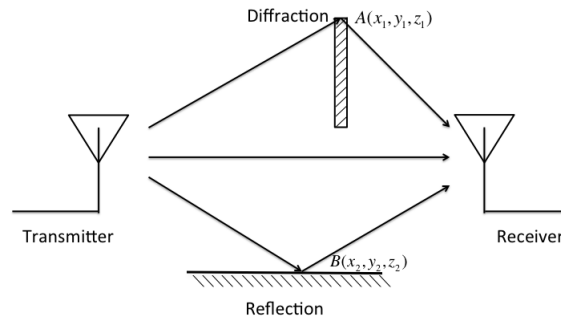


**Figure 2.3:** Radio waves transmission, reflection, and diffraction;  $A(x_1, y_1, z_1)$  diffraction point,  $B(x_1, y_1, z_1)$  reflection point.

In this work, the ray-tracer used for simulation is *Wireless Insite* (WI). *X3D Ray* model and *Urban Canyon* model are two propagation models provided by WI. These two propagation models simulate propagation paths in cooperation with ray-tracing algorithm and *Uniform Theory of Diffraction* (UTD), an extension method of *Geometrical Theory of Diffraction* (GTD); but these two models have the different characteristic, limits, and electric field evaluation [19]. The X3D model is used in the indoor simulation, because it is able to run on a GPU and make use of multi-threading; this benefit saves plenty of time in the indoor simulation with so many details. The *Urban Canyon* model is design for the outdoor simulation in which the height of the transmitter and receiver is not comparable with the building height; the rays propagated between buildings are focused while the rays transmitted over the roof are ignored [19].

The *Shooting and Bouncing Ray* (SBR) method described in [19,29,30] is used in both propagation models. In SBR, a source point shoots rays with certain angle spacing ( $0.2^\circ$  recommended by [19] for most situations) and traces the propagation paths which ends at a collection sphere (a circle around the field point) [19].

The measurement procedure and ray-tracing simulation are introduced in detail in this chapter. Only the indoor 15 GHz MISO channel and 28 GHz  $49 \times 49$  MIMO channel were measured to compare the PDP and received power with the indoor simulation results. Based on that, the outdoor ray tracing model is built to observe channel performances at 15 and 28 GHz. Different virtual models are simulated to explore the effect of material permittivity and the level of geometric details needed in simulation.

In the ray-tracer, the indoor virtual scenario should be as similar as possible to the room where the real measurements are carried out. The geometry of the conference room and all objects inside were measured and simulated as detailed as possible. The outdoor virtual scenario directly comes from a three-dimensional map containing terrain and building blocks. Detailed objects, for example, windows, stairs, and cars are added later on based on google maps.

### 3.1 Synthesised antenna pattern

The channel is simulated as a SISO link with isotropic antenna utilised at both transmitting and receiving sides. Simulation with isotropic SISO channel makes it possible to construct different antenna structures: (1) antenna element patterns, for example, patch, monopole, or dipole pattern; (2) antenna array geometries, such as a linear array or an  $8 \times 32$  two-dimensional array.

#### 3.1.1 Synthesised antenna array pattern

In the ray-tracer, a  $1 \times 8$  MISO system is created to verify the feasibility of replacing the simulated array with the synthesised array. A simulated array stands for the antenna array which is built in the ray-tracer while the synthesised array means a virtual array generated from the simulation of a single antenna by adding phase shift. That is, applying phase shifts on the SISO channel plane waves derives the plane waves of a synthesised MIMO array. The original antenna element in the synthesised array where other plane waves are derived from is exactly the same with one of the antenna element in the simulated array. In the experiment, as it is shown in figure 3.1, the antenna elements have distance spacing  $\lambda/2$  with each other, and all elements align linearly on  $\hat{x}$ -direction. In this case, the first antenna

element in the simulated array is chosen as the original antenna of the synthesised array, so that the data of the first element in simulated array and in synthesised array are the same. The plane wave data of the second and third antenna elements are generated by applying corresponding phase shift on every plane wave of the original antenna element.

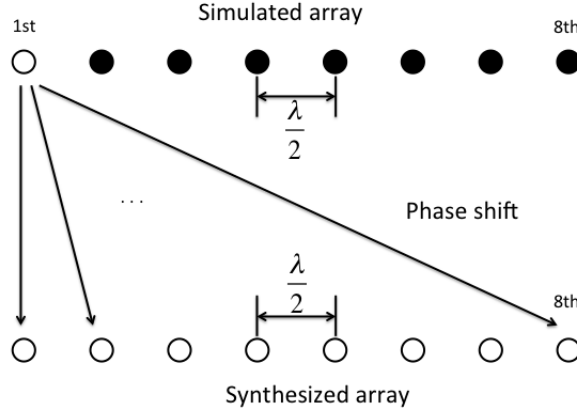


**Figure 3.1:** Synthesising the virtual antenna array by the first element of the simulated array.

To have a better explanation, an antenna element position is represented by  $(d\hat{x}, d\hat{y}, d\hat{z})$  and assume the first antenna element is the origin  $(0, 0, 0)$ ; the *Angle of Departure* (AOD) of the  $i$ th plane wave is  $AoD_i(\phi, \theta)$ , and  $a_k$  is the antenna gain of the  $k$ th element, for example  $a_k = 1$  for all plane wave directions if it is isotropic antenna; also  $f_c$  is the carrier frequency, and  $c$  is the speed of light. The phased array factor  $A(\hat{\mathbf{r}})$  of antenna elements is expressed as:

$$A(\hat{\mathbf{r}}) = a_k \exp\left(j2\pi f_c \frac{d\hat{\mathbf{r}}}{c}\right), \quad (3.1)$$

and

$$d\hat{\mathbf{r}} = \sin\theta \cos\phi d\hat{x} + \sin\theta \sin\phi d\hat{y} + \cos\theta d\hat{z}. \quad (3.2)$$

It is the same method when synthesising antenna array pattern at receiver side, but the AOD of plane waves is replaced by AOA. In this way,  $A(\hat{\mathbf{r}}_{k,i})$  describes the phase shift of the  $i$ th plane wave seen by the  $k$ th antenna element.  $A_a(\hat{\mathbf{r}})$  and  $A_d(\hat{\mathbf{r}})$  represent phase array factors of the receiver with AOA and of the transmitter with AOD, correspondingly. In the MIMO channel, phased array factors  $A_a(\hat{\mathbf{r}})$  and  $A_d(\hat{\mathbf{r}})$  affect the channel in a same way due to antenna reciprocity. The variable  $A_{(m,n)}$  denotes the phase shift on the both sides of the  $i$ th plane wave, and is represented as:

$$A_{(m,n)} = A_a(\hat{\mathbf{r}}_{m,i}) A_d(\hat{\mathbf{r}}_{n,i}), \quad (3.3)$$

where  $m$  is the antenna element index of receiver array, while  $n$  is the index of transmitter array. In this way,  $A_{(1,1)}$  is the phase shift of the pair of the first antenna element in the receiving array and the first element in the transmitting

antenna array. As the position of the first element in the array is also used as the origin position, the relative distances are zero at both sides, then the  $A_{(1,1)}$  is equal to 1 if the isotropic antenna pattern is assumed. The phased array factor of the  $M_R \times M_T$  MIMO of the  $i$ th plane wave is expressed as:

$$\mathbf{A}_i = \begin{bmatrix} A_{(1,1)} & A_{(1,2)} & \cdots & A_{(1,M_T)} \\ A_{(2,1)} & A_{(2,2)} & \cdots & A_{(2,M_T)} \\ \vdots & \vdots & \ddots & \vdots \\ A_{(M_R,1)} & A_{(M_R,2)} & \cdots & A_{(M_R,M_T)} \end{bmatrix}. \quad (3.4)$$

### 3.1.2 MIMO transfer function of the synthesised array

In the simulation, it is the plane wave data calculated by the ray-tracer. Assuming the vector  $\mathbf{p} = (p_1, p_2, \dots, p_i, \dots, p_l)$  is a SISO link plane wave sequence,  $p_i$  is the  $i$ th plane wave which contains the following properties: received power  $p_{r,x,i}$ , phase  $\Phi_i$ , time of arrival  $t_i$ , angle of arrival  $AoA_i (\theta', \phi')$ , and angle of departure  $AoD_i (\theta, \phi)$ . The sequence length is  $l$  and it is also the number of rays, obviously. At 15 and 28 GHz, wavelengths are in millimeter scale, and antenna spacing of the array is half of the wavelength. Comparing with the distance between the base station and receivers, for example in the outdoor scenario the distance range is from 5m to 150m around, the antenna element position difference due to spacing is trivial so that the direction of one plane wave seen by other synthesised elements can be regarded the same. That means, one plane wave's  $AoD$  of the transmitting array is assumed identical to all antenna elements in that array, and also the same assumption with the  $AoA$  of the receiving array.

The complex amplitude  $\alpha$  of one plane wave is calculated as:

$$\alpha = p_{r,x} e^{j2\pi\Phi} \quad (3.5)$$

Although the subtle position difference of antenna elements does not have a significant influence on the plane wave's direction, it has a major impact on the plane wave's phase and therefore affects the complex amplitude. By multiplying the complex amplitude and the phased array factor  $\mathbf{A}_i$  of the  $i$ th plane wave together, plane waves of the synthesised antenna array are expressed as:

$$\boldsymbol{\beta} = (\alpha_1 \mathbf{A}_1, \alpha_2 \mathbf{A}_2, \dots, \alpha_i \mathbf{A}_i, \dots, \alpha_l \mathbf{A}_l) \quad (3.6)$$

If a synthesised  $M_R \times M_T$  MIMO array is simulated with  $l$  rays, then the plane waves' complex amplitude of the whole array is a  $M_R \times M_T \times l$  three dimensional matrix. Based on that, the channel transfer function is derived from *Fourier transformation* and is described as [15]:

$$h(k) = \sum_{i=1}^l \beta_i e^{-j2\pi\Delta f t_i k}, \quad (3.7)$$

where  $k$  is the index of frequency points of interest. Usually, the number of frequency points is decided by the system bandwidth and maximum delay. Assuming  $N$  stand for the number of frequency points in the case, the size of the channel transfer function matrix is  $M_R \times M_T \times N$ .

Figure 3.2 shows the PDP comparison of the simulated array and synthesised array. The solid line *Syn* stands for the PDP of synthesised array and cross *RT* means the PDP of simulated array. It is easy to notice from the figure that the difference between PDP shapes of the simulated array and synthesised array is trivial enough that the result of the synthesised array is a reasonable replacement of the simulated array results.

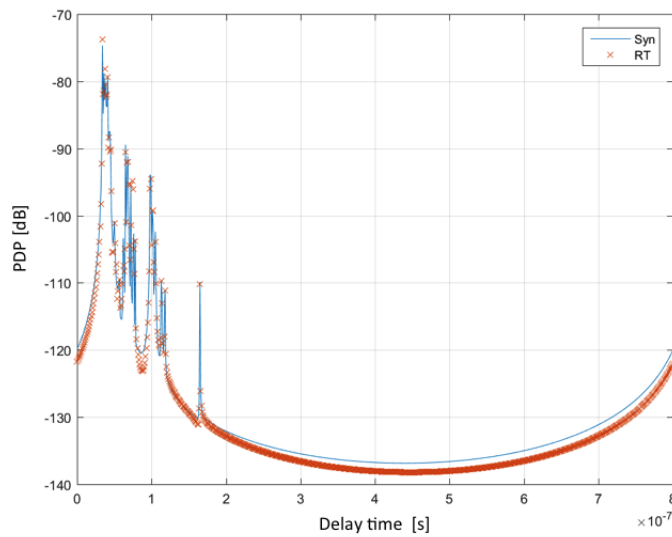


**Figure 3.2:** The PDP comparison of the simulated antenna array and synthesised antenna array.

### Implementing antenna element pattern

As it was mentioned before, in the ray-tracer, the isotropic antenna element works at the transmitter side and receiver side. To also observe the channel under the effect of a patch antenna element, the isotropic antenna pattern is replaced by the patch antenna pattern as figure 3.3 shows. When the isotropic antenna is utilised, plane waves  $p_1$ ,  $p_2$ ,  $p_3$ , and  $p_4$  coming from different directions are perceived and have the same antenna gain. With the patch antenna pattern applied, the plane wave  $p_2$  has the strongest antenna gain while the plane wave  $p_4$  is not perceived. It is the same principle if the monopole pattern is adopted.

Apparently, only by simulating the channel with the isotropic antenna, plane waves from all directions are discerned, which makes it possible to implement different antenna patterns for future use. If it is the patch antenna element used in the simulation, plane waves, such as  $p_4$ , cannot be identified since the antenna gain at that direction is zero or close to zero. Even if the antenna pattern applied later on has strong gains at directions where plane waves are not detected before, for example  $p_4$  under patch element simulation in this case, plane waves from those

directions are not able to be restored due to the lack of original data, and therefore it brings in errors to the simulation results.

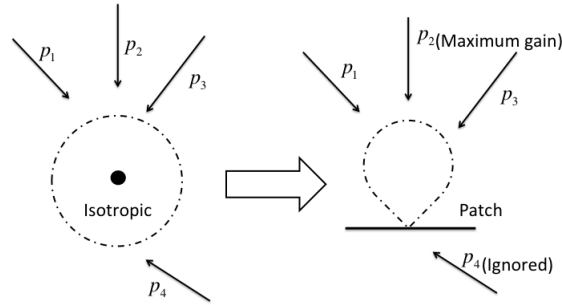


**Figure 3.3:** Replacing the isotropic antenna pattern with the patch antenna pattern.

### 3.2 Indoor scenario properties

The indoor channel model is built to verify the accuracy of the ray-tracer by comparing the PDP shape based on measurement data with the PDP from simulation results. The system bandwidth, noise figure, room temperature, and other parameters are shown in table 3.1.

**Table 3.1:** Indoor communication system of 15 and 28 GHz

Name	Value
Bandwidth	800 MHz
$P_{tx}$	0 dBm
NF	10 dB
Temperature	290 K
Noise power	-105 dBm
CMR threshold	-75 dBm
Frequency points	801

At 15 GHz, the indoor system model is a MISO system with a single monopole as receiver and a  $10 \times 10$  two-dimensional patch array as transmitter placed vertical to the ground. The patch antenna pattern is shown in figure 3.4, which is also used in the outdoor simulation. The monopole antenna pattern is shown in figure 3.5.

At 28 GHz, a  $49 \times 49$  MIMO system is measured; and at both sides, the antenna structure is  $7 \times 7$  two-dimensional monopole array. The transmitter array is oriented vertical to the ground and the receiver array is parallel to the ground. All

monopole antennae are placed vertically. The 28 GHz monopole antenna pattern is derived from the 15 GHz monopole pattern because the measured monopole pattern of 28 GHz was not available at the time of publication. The monopole antenna gain at azimuth plane of the 15 GHz is measured; and it is used to scale the 15 GHz monopole pattern in order to generate the 28 GHz monopole pattern.

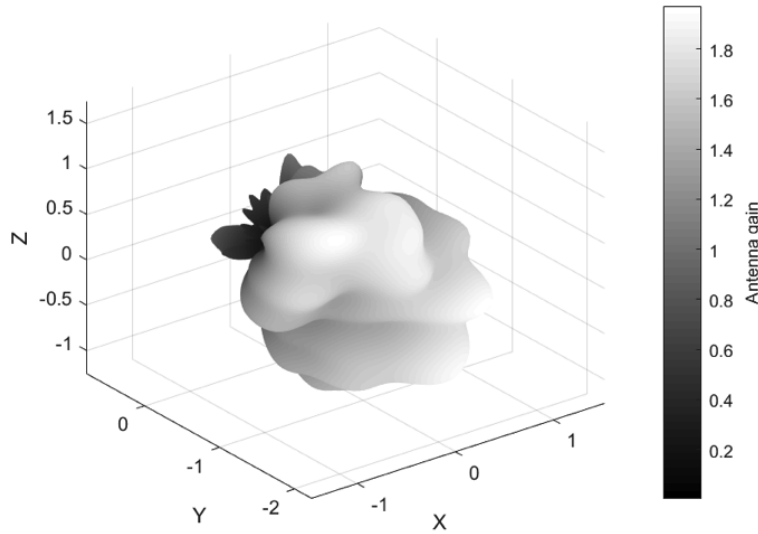


**Figure 3.4:** Patch antenna pattern.

### 3.2.1 Material permittivity measurement

The relative permittivity  $\epsilon_r$  is also known as the dielectric constant which reflects the material influence on the electric field and is dependent on the frequency [31]. In most ray-tracing simulations [8, 11–13, 32, 33], relative permittivities are approximate values, which fail to represent the real environment and can lead to inaccurate prediction of simulation results. To emulate the radio wave transmission as much as possible, the material permittivities of indoor objects are measured using method in [34] with horn antenna at 15 GHz and lens leaky antenna at 28 GHz. This analysis and measurement were performed in a separate work at LTH, and results are not yet published.

The material permittivity property in the ray-tracer is represented by two parts:  $\epsilon'_r$  the real part of the relative permittivity, and  $\sigma$  (S/m) the conductivity describing the relative permittivity’s imaginary part  $\epsilon''_r$  [19]. The conversion between the conductivity  $\sigma$  and the imaginary part of the relative permittivity  $\epsilon''_r$  is expressed as:

$$\sigma = \epsilon_0 \epsilon''_r \omega \quad (3.8)$$



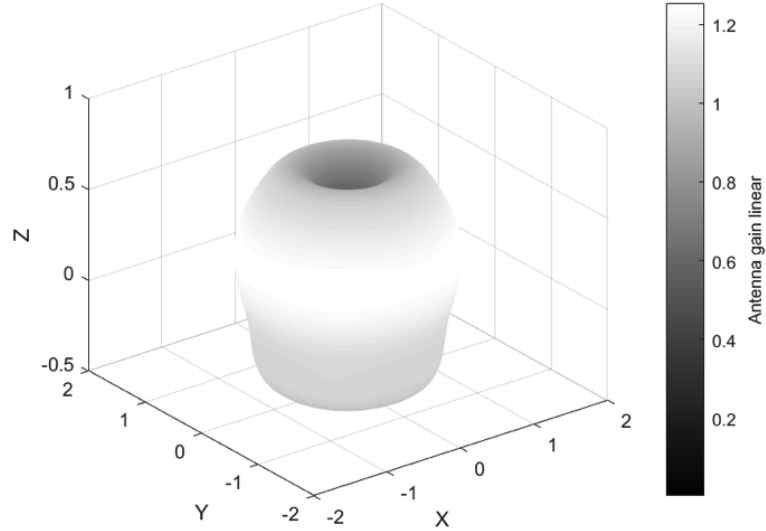


**Figure 3.5:** Monopole antenna pattern of 15 GHz

where  $\omega$  is the angular frequency of the transmission carrier frequency, and  $\epsilon_0 = 8.8542 \times 10^{-12}$  F/m is the vacuum permittivity. Table 3.2 shows the relative permittivity based on the measurement result, and these values are used in the ray-tracing simulation. Other materials whose permittivities are difficult to be measured by the method in [34], for example the concrete of the floor, the coating layer of the ceiling, are set to be the theoretical values according to [35].

**Table 3.2:** Indoor material measured permittivities

Material	15 GHz		28 GHz	
	$\epsilon'_r$	$\sigma(S/m)$	$\epsilon'_r$	$\sigma(S/m)$
Door (wood)	1.637	0.0812	1.621	0.0953
Table(wood)	1.931	0.0921	1.885	0.1143
Chair(wood)	2.250	0.1049	2.197	0.1429
Plaster	2.371	0.0154	2.366	0.0143
Wall	5.041	0.2523	5.041	0.3287

### 3.2.2 Indoor geometry and parameters in the ray-tracer

Figure 3.6 shows the detailed three-dimensional virtual conference room model at 15 GHz in the ray-tracer. Figure 3.7 is the two-dimensional sky view. The green cube is the transmitter and the red cubes stand for receivers. All receiver locations shown in figure 3.7 have measurements, though in this work, the measured results of Rx1, 2, 3, and 4 are used. The ceiling and walls exist but are invisible so that objects inside the room can be seen. The Indoor 28 GHz model has the same geometry, but with different material permittivities and different transmitter, receiver positions.

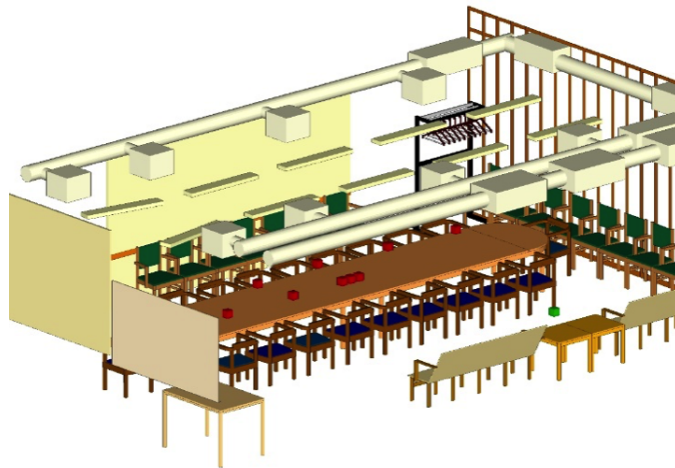


**Figure 3.6:** Indoor 15 GHz detailed three-dimensional model in the ray-tracer

As it was mentioned before, in all the ray-tracing simulations, it is the isotropic SISO link used in the system. Table 3.3 shows other settings in the ray-tracer; these values are determined according to the WI reference manual [19].

**Table 3.3:** Indoor parameters in ray-tracer

Name	Value
Ray number	200
$P_{tx}$	0 dBm
Antenna noise figure	3 dB
Model	X3D
Reflection order	6
Diffraction order	1

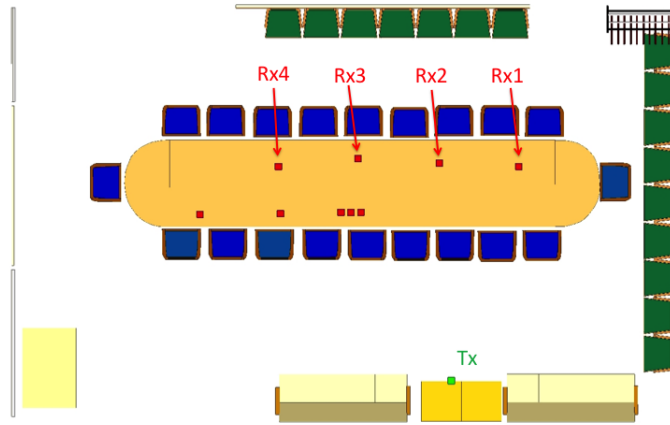


**Figure 3.7:** Indoor 15 GHz two-dimensional sky view in the ray-tracer

Besides the detailed indoor three-dimensional model shown in figure 3.6 which contains chairs, ventilations, hangers, and ceiling lamps, a much simpler indoor model shown in figure 3.8 is created to explore the influence of level of geometric details on the simulation results. The objects, such as tables, windows, doors, and floor, use the same permittivity values as shown in table 3.2. To distinguish these two models, the result of the simple indoor model will be noted as *Indoor simplified model*, and the result without any model type specified is simulated by the detailed model which is regarded as the default model.

### 3.3 Indoor measurement

The conference room where the measurement took place is a static scenario, since the moving virtual array method is conducted in the measurement. In this method, the virtual array is constructed by moving antenna element to a different position each time; the benefit is that only one pair of antenna is needed in the measurement and antenna array is not necessary; but since every single channel is measured one by one, the virtual array measurement takes a lot of time [20], especially when the antenna array has a large number of elements.

Since at 15 GHz, the channel is a  $1 \times 100$  MISO system with 1 GHz bandwidth, the *Vector Network Analyser* (VNA) measured the channel transfer function from frequency 14.5 to 15.5 GHz and repeated this process 100 times. Comparing to the indoor 15 GHz scenario in which the channel of four receiver positions are chosen to be measured, the  $49 \times 49$  MIMO channel measurement with a 10 GHz bandwidth at 28 GHz, from 22 to 32 GHz, takes a much longer time so that only one receiver’s position is chosen.

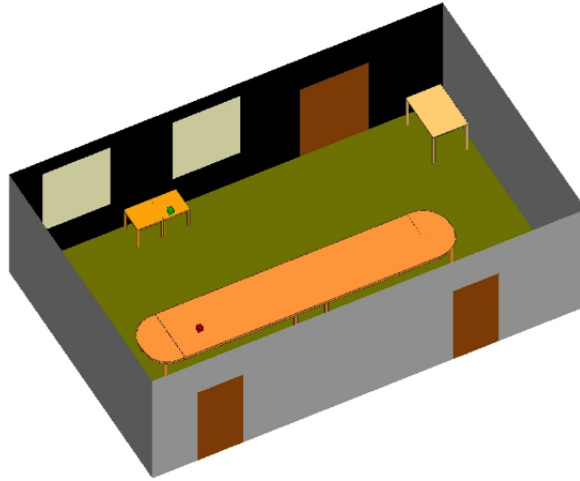


**Figure 3.8:** Indoor 15 GHz simplified three-dimensional model

## 3.4 Outdoor scenario properties

The outdoor model is mainly simulated with building blocks constructed by different materials, such as brick or concrete. Detailed objects, such as window frames, doors, parking cars, and metal stairs are also created. The outdoor communication system has a transmitting power of 31.5 dBm which is the only different one from parameters of the indoor communication system in which the transmitting power is 0 dBm. This is because, in the outdoor environment, the transmission distance is much longer than the one in the indoor scenario, thus the transmitter in the outdoor case sends signals with a higher power. Other parameters of the outdoor communication system are the same with those values in table 3.1. In terms of settings of the ray-tracer, the outdoor simulating model is changed to be *Urban Canyon*, and other parameters are the same with those in table 3.3. The channel simulation is processed as a SISO link with an isotropic antenna element as well.

Besides the MIMO channel with the isotropic antenna, the outdoor model is also observed when a patch antenna element is utilised. The patch antenna pattern replaces the isotropic antenna pattern as section 3.1.2 describes, and its pattern is shown in figure 3.4 already. The patch pattern that radiates at north is implemented at the transmitter antenna array; and at the receiver side, the patch antenna radiates to the south. More details of applying two different radiating direction antennae are explained in section 3.4.2.

### 3.4.1 Outdoor geometry

The real environment of the outdoor channel is an area located in Kistagangen, Stockholm, Sweden shown in figure 3.9; where *Street Route (ST)* area is the group

of receivers placed along the streets. The red line in a yellow dash ellipse is named *Street Route 1* (ST1). This street line is specially mentioned because it demonstrates the transmitter’s patch antenna array radiating direction which is vertical to this route. Figure 3.10 is the simulation environment in the ray-tracer; the positions of the transmitters are marked by crosses, and all receiver positions are marked by square points. The transmitter height is 8.5 m consistent with [16]. Receivers except those in the ST area are grouped into the NLOS area where every receiver do not have LOS component from the transmitter. In figure 3.11, detailed objects, for instance windows, doors, cars, and stairs, which are considered having effects on scatters, are also modelled.

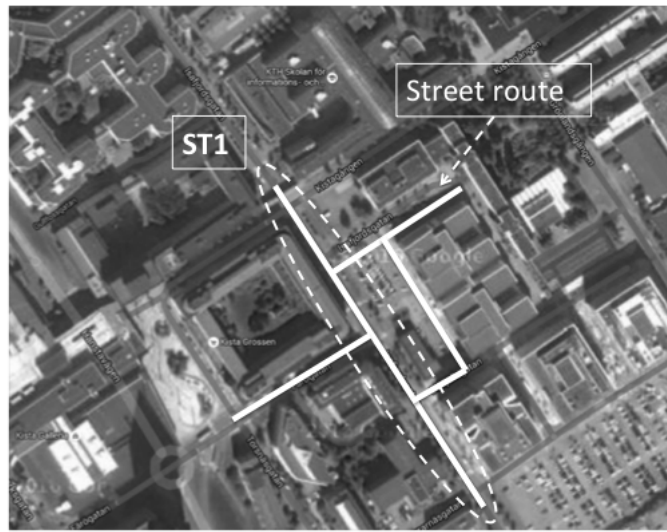


**Figure 3.9:** Outdoor real environment Kistagangen, Kista, Stockholm.

Same with the indoor scenario, to find out the influence of the level of geometric details on the simulation result, a simple outdoor simulation model without detailed objects is created; the building material permittivities are the same with the values in the outdoor detailed model, with permittivities as in table 3.4. Furthermore, to understand the effect of the material permittivity, another simplified outdoor model is created with the same geometric structure of the *simple outdoor model* but with a consistent building block material concrete, see figure 3.12, named as simple concrete model. In a word, the *simple model* has the same building structures as the *simple concrete model* but the same material permittivity as the detailed car model. The material permittivity of the concrete in the simple concrete model is the default concrete value from [19], which is different from the concrete permittivity value in table 3.4, and its relative permittivity is  $\epsilon = 15$  and the conductivity is  $\sigma = 0.015$  S/m. The terrain is the same with the one in figure 3.11, but is invisible in figure 3.12. The comparison among three different models is only carried out in the 15 GHz frequency band. Same as in the indoor case, any outdoor results without model type specification is based on the detailed outdoor

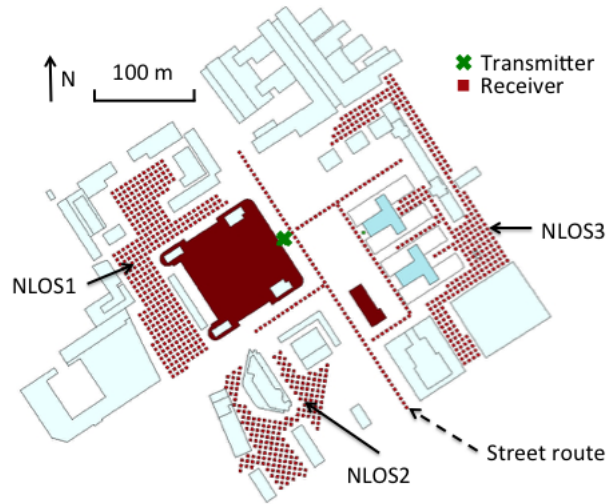


**Figure 3.10:** Outdoor virtual model sky view in the ray-tracer.

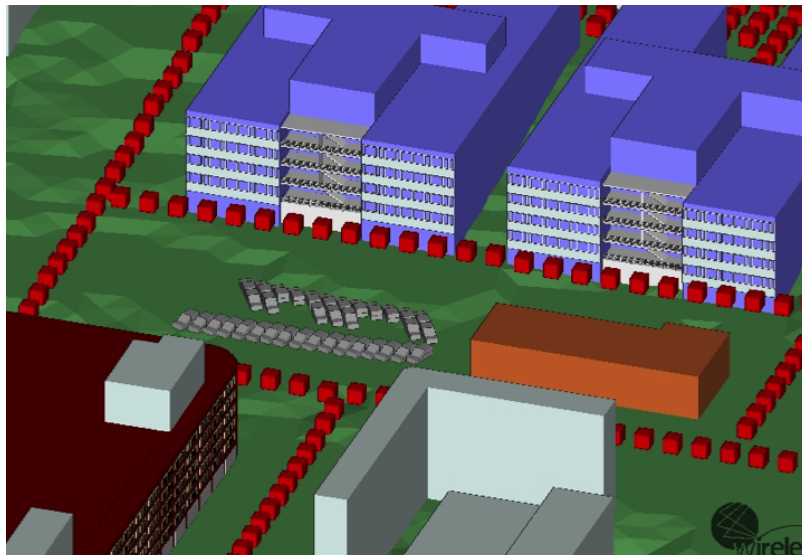


**Figure 3.11:** Outdoor three-dimensional detailed car model in the ray-tracer

model, known as *detailed car model* in the model results comparison.

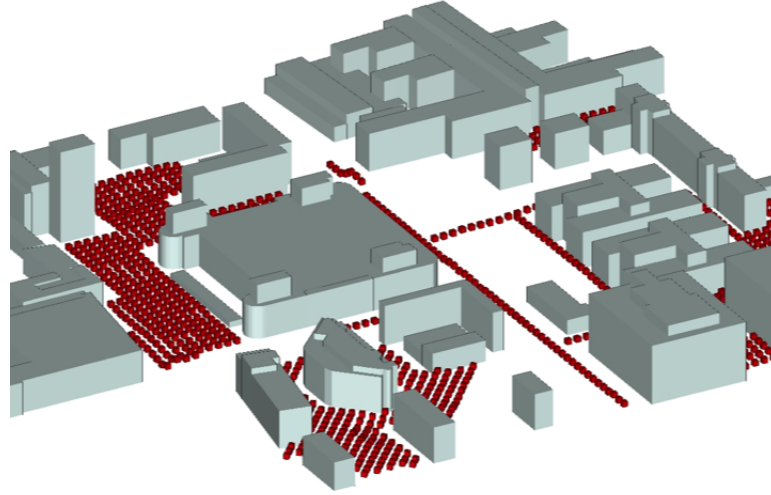


**Figure 3.12:** Outdoor 15 GHz simplified model with concrete building blocks

### 3.4.2 Antenna array alignment and geometry

An  $8 \times 32$  MIMO system is synthesised based on the data of the outdoor SISO simulation, and four antenna processing techniques: beamforming (directional beamforming and DET), spatial multiplexing, HB2, and HB4 are utilised. In all four cases, the base station uses the same antenna array structure as figure 3.13 shows, receivers' antennae are an 8 element linear array in figure 3.13. The base station antenna is a  $4 \times 8$  two-dimensional array with 4 antenna elements aligned on  $\hat{x}$  direction and 8 antenna elements placed on  $\hat{z}$  direction. And it rotated around the  $\hat{z}$  axis so that its alignment on  $\phi$  plane is parallel to the ST1 street line. If the patch antenna pattern which radiates north is implemented, its radiating direction is vertical to the ST1. The receiver antenna array is aligned along  $\hat{x}$  direction without any rotation. And the patch antenna pattern added on the receiver radiates to south.

### 3.4.3 Building material properties

Buildings in the outdoor environment are constructed by different materials, such as brick, concrete, metal, or glasses, and therefore has various influences on the radio waves. The value of material relative permittivity and conductivity in the ray-tracer come from ITU building material measurements [35]. The five materials' dielectric constant estimated values are the same at 15 and 28 GHz according

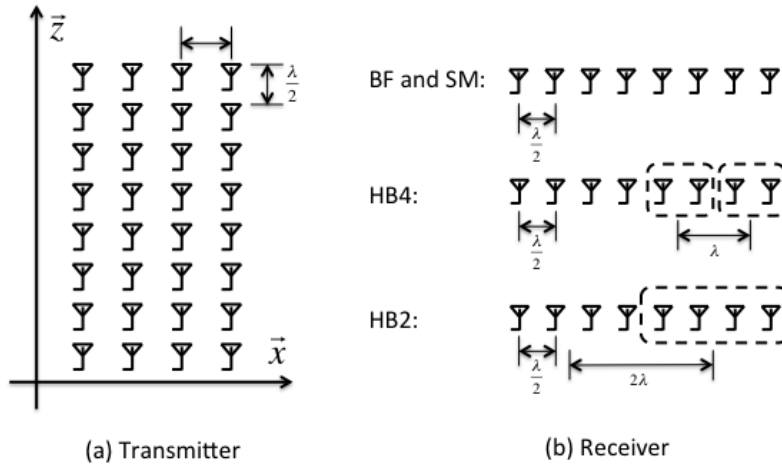


**Figure 3.13:** Outdoor MIMO antenna array structure

to [35]. Table 3.4 shows the material conductivity and the real part of relative permittivity value used in the outdoor simulation.

**Table 3.4:** Outdoor detailed car model material permittivity and conductivity

Material	Dielectric constant		Conductivity $S/m$	
	15 GHz	28 GHz	15 GHz	28 GHz
Concrete	5.31		0.2919	0.4838
Brick	3.75		0.038	
Metal	1		$10^7$	
Glass ( normal )	6.27		0.1086	0.2287
Glass ( metallic )	6.27		15	
Wood	5		0	
Terrain ( dry ground)	3		0.1380	0.6652



## Indoor measurement and simulation comparison

---

At 15 GHz, the channel measurement took place at the Rx1, Rx2, Rx3, and Rx4. For the channel of Rx1, the *Obstructed Line-of-sight* (OLOS) scenario is also measured when an phantom is placed to block the LOS component in order to figure out the received power loss caused by the obstructed object. The PDP, AOD, and received power comparisons of 15 GHz channel between the simulation and measurement are presented in this chapter. At 28 GHz, only the PDP comparison is shown.

From figure 4.1, the channel richness distribution of 15 GHz, the outline of a meeting table in the room is roughly observed, see figure 3.7 for the position of the table. The channel richness colour on the table region is darker than the area around. This is because, in the simulation, receivers were placed 15 cm higher than the meeting table. The plane waves reflected by the table and perceived by the receivers above the table are hard to be distinguished from LOS components in an 800 MHz bandwidth system, and thus are not counted into the channel richness.

In figure 4.2, which is the 15 GHz channel multiplexing richness distribution of the simplified indoor model, the colour scale is consistent with the scale in figure 4.1 to have a clear comparison, but the maximum richness value is only 6. Reflected and diffracted plane waves produced by chairs, ventilations, and lamps disappeared.

The channel multiplexing richness distribution of 28 GHz is shown in figure 4.3. Unlike the richness distribution of 15 GHz, no objects' outline is observed at 28 GHz frequency. The channel richness colour scale of 28 GHz is not consistent with the range of 15 GHz, otherwise the distribution shape is not clear. The maximum channel richness value of 28 GHz is 5 which is even lower than the max CMR of 15 GHz simplified model, and only portion of receivers which are located close to the wall behind the transmitter show a strong scattering rich effect.

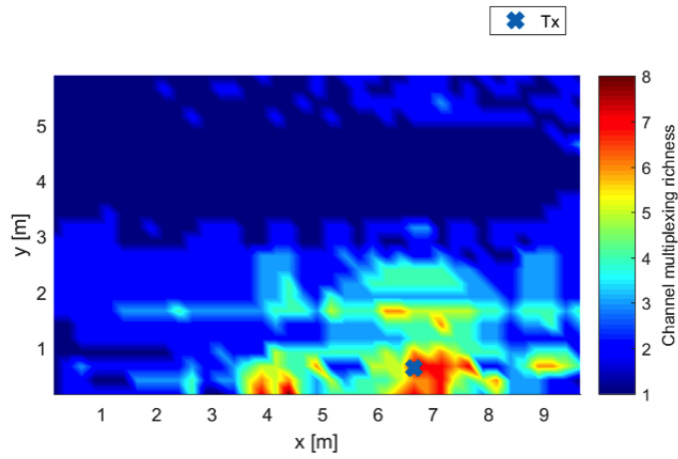


**Figure 4.1:** Indoor 15 GHz channel multiplexing richness

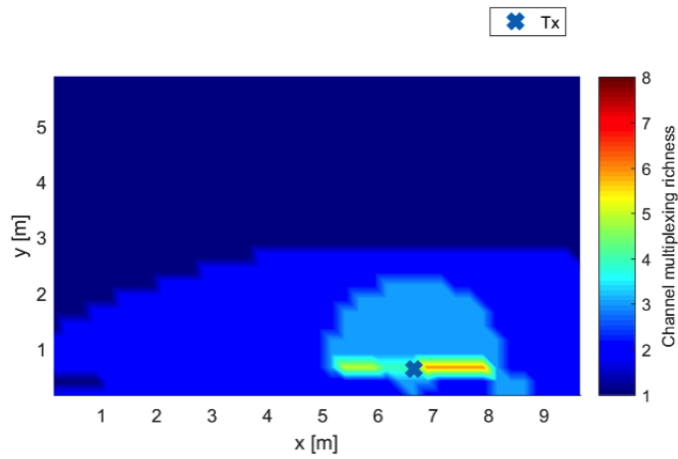


**Figure 4.2:** Indoor simplified model channel multiplexing richness

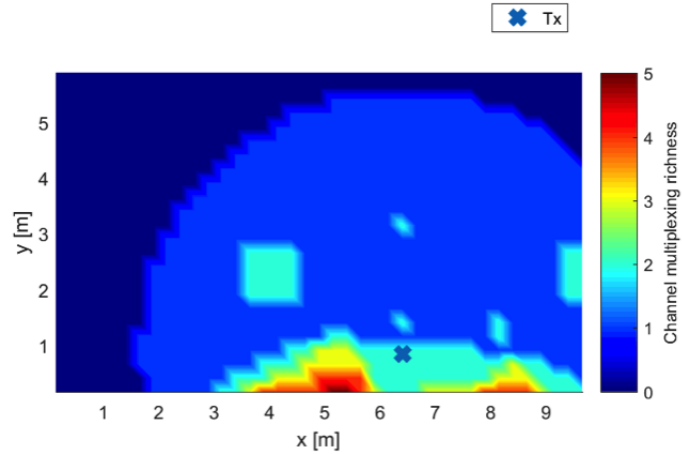


**Figure 4.3:** Indoor 28 GHz channel multiplexing richness

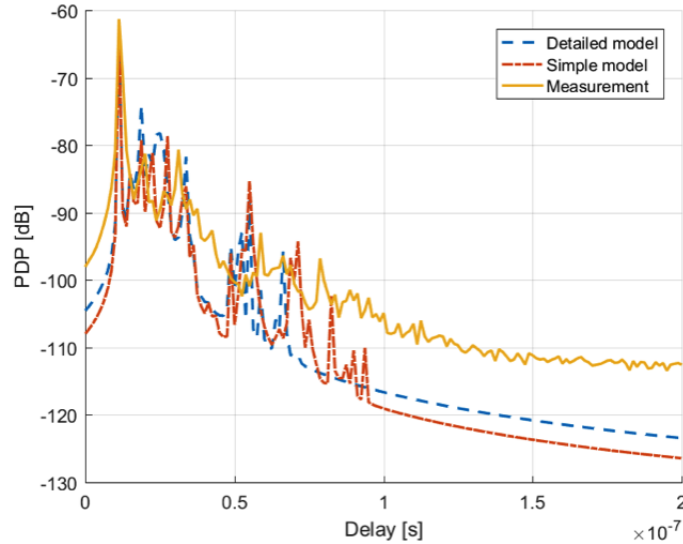
#### 4.1 Indoor 15 GHz $1 \times 100$ MISO PDP and received power

Figure 4.4 shows the magnified PDP shape comparison of Rx1 at 15 GHz for the measurement, the detailed indoor model, and the simple indoor model. The PDP comparisons of Rx2, 3, and 4 are attached in appendix. For all four receivers, the delay time of the peak value is around 3.75 ns later than the simulation delay time which is due to the extra path length caused by transmission lines in the antennae. This delay error is compensated in all the PDP comparison figures. At Rx1, the PDP peak value of the measurement and simulation are quite close. The PDP comparisons of Rx2, Rx3 and Rx4 in appendix, however, show that the PDP peak value in the simulation is around 5 to 6 dB higher than the peak value of the measurement. As the measurement bandwidth of 15 GHz is 1GHz which is not able to resolve all plan waves, and the diffuse part of the PDP is not captured by the ray-tracer, the PDP difference between the simulation and measurement is expected.

**Table 4.1:** Indoor 15 GHz MISO DET received power comparison

Received power [dBm]	Rx1	Rx2	Rx3	Rx4
Simulation	-61.81	-59.53	-59.91	-63.28
Measurement	-59.92	-67.71	-63.77	-65.31

The received power comparison of the simulation and measurement data of four receivers are shown in table 4.1. The received power differences of Rx1 and



**Figure 4.4:** Indoor 15 GHz PDP Rx1 comparison of the measurement and two simulation models

Rx4 between the simulation and measurement are adequate, -1.89 dB at Rx1 and 2.03 dB at Rx4. The largest difference occurs at Rx2 which is up to 8.18 dB. To observe the influence of an obstructor on the received power, a phantom is placed on the path between Tx and Rx1 to block the LOS component. The result is shown in table 4.2. The measurement has a 4.23 dB higher obstructed power loss than the simulation.

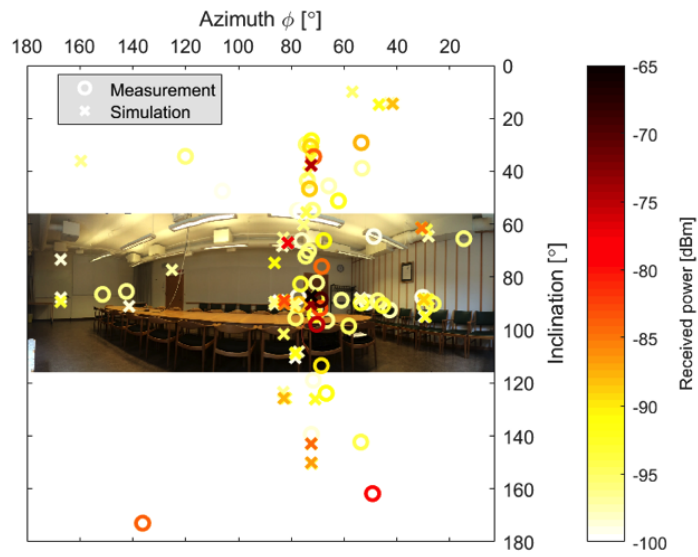
**Table 4.2:** Indoor 15 GHz MISO received power Rx1

	LOS [dBm]	OLOS [dBm]	Loss [dB]
Simulation	-61.81	-68.58	6.77
Measurement	-59.92	-70.92	11.00

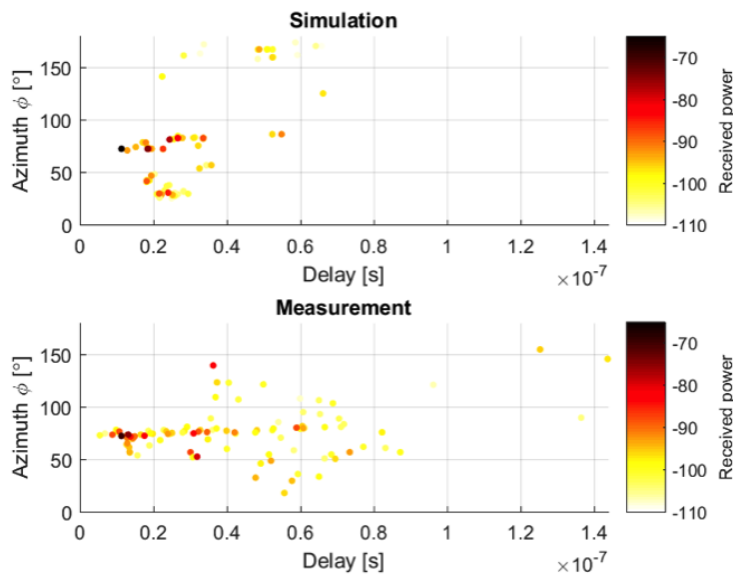
At 15 GHz, the radio wave AODs of the  $10 \times 10$  two-dimensional patch array are estimated based on the measurement data. Figure 4.5 shows the AOD comparison of Rx1, in which the circle are the plane wave direction of departure estimated from the measurement, and the cross are the simulation AOD, see Rx1 position in figure 3.7. The colour of each marker indicates the power a plane wave carrying with. In the direction that  $\phi$  angle is  $75^\circ$  around, the allocation of crosses and circles overlaps to a great extent, which means the AODs of the simulation and measurement agree with each other fairly well.

From figure 4.5, in the measurement, there are more rays whose delay time is

greater than 50 ns. This is because, in the real scenario, the surfaces of objects, such as chairs, tables and doors, are rough, and their material permittivities are inconsistent. In the ray-tracer, however, it can not accurately simulate the surface roughness so that scatterings caused by these irregular variations, i.e diffuse scattering are ignored. It is expected that the measurement shows more multipath components than the simulation result.



(a) View from transmitter



(b) Angular spread with delay time

Figure 4.5: Indoor 15 GHz AOD Rx1

## 4.2 Indoor 28 GHz $49 \times 49$ MIMO PDP

Figure 4.6 is the PDP comparison of the  $49 \times 49$  MIMO indoor channel at 28 GHz. As the frequency range in the measurement started from 22 GHz and ended at 32 GHz, a 10 GHz bandwidth is wide enough to distinguish every signal spikes. In figure 4.6, the PDP shape is also magnified as the same reason of the indoor 15 GHz case. The peak values of the measurement and simulation only have a less than 2 dB difference, and their corresponding delay times are close. Also, the plane wave's received power is plotted in the figure. As the transmitting power is 0 dBm, the received power of each ray is expected to be consistent with PDP in number but with a different unit (dBm in figure 4.6).

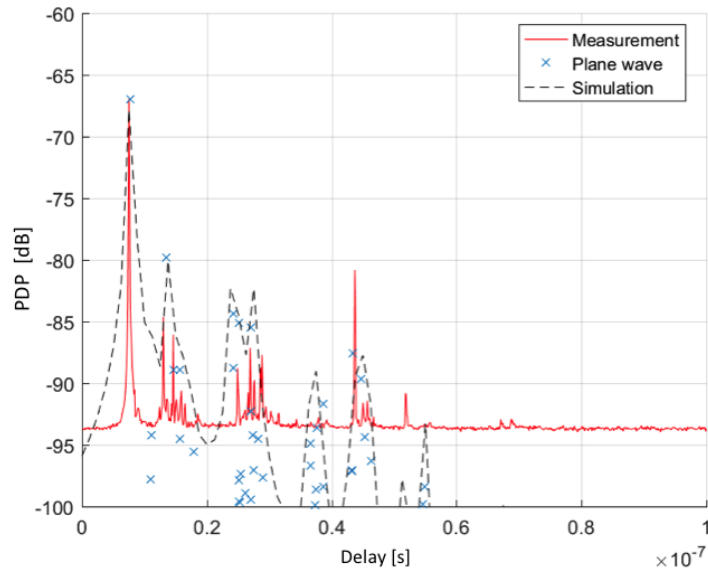


**Figure 4.6:** Indoor 28 GHz PDP comparison





## Outdoor scenario channel characteristics

In the outdoor scenario, the positions of the transmitter and receivers have already been shown in figure 3.10. This chapter shows the channel properties, the channel multiplexing richness of a SISO isotropic system, the RMS delay spread of an  $8 \times 32$  MIMO isotropic system, and the received power of a  $1 \times 32$  MISO patch and monopole system. The RMS delay spread is observed with the isotropic antenna element in order to eliminate the influence of the antenna pattern. The outdoor MISO received power is synthesised with the patch and monopole antenna element to imitate the outdoor 15 GHz signal strength measurement by Ericsson in [16,36].

### 5.1 Channel multiplexing richness

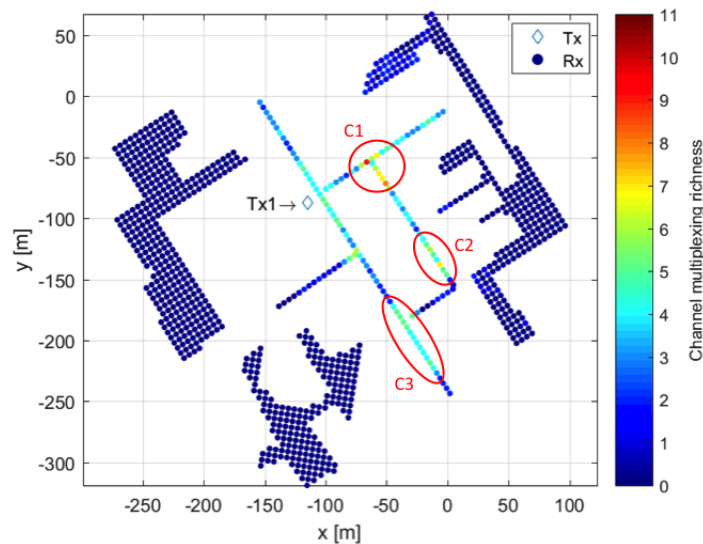


**Figure 5.1:** Outdoor 15 GHz SISO isotropic antenna element CMR distribution

Figure 5.1 and figure 5.4 show the channel multiplexing richness(CMR) of the

SISO system with the isotropic antenna element of 15 and 28 GHz. The two figures, 5.2 and 5.3, show the CMR 15 GHz distribution of the simple concrete model and the simple model. Since the CMR is observed without any antenna influence, neither the antenna pattern or array pattern, it reflects the effect that the environment has on the radio wave. As it was introduced in section 3.4.1, the differences among the simple model, the simple concrete model, and the detailed car model are the material permittivity and level of geometric details. Again, the level of geometric details is a contrast between the simple model and the detailed car model; in the simple concrete model, even the material permittivity of the building block is different.

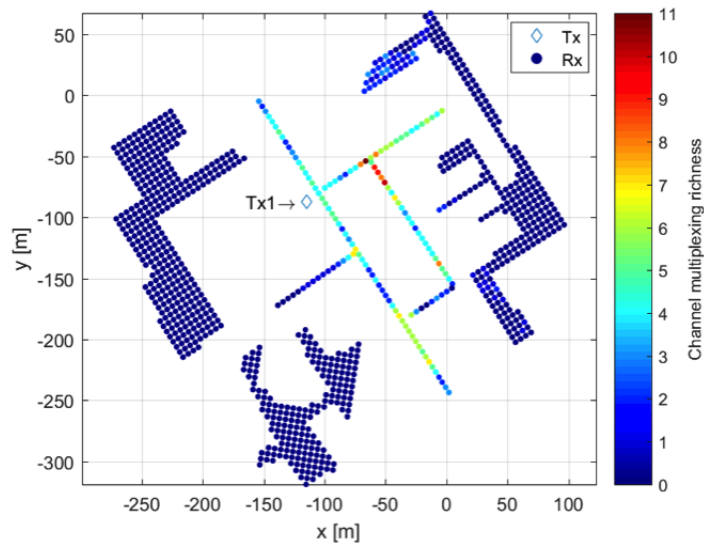


**Figure 5.2:** Outdoor 15 GHz *Simple concrete model* CMR distribution

Comparing the CMR 15 GHz distribution of these three different models, it is noticed that the simple model shows an obvious smaller scattering richness than the detailed car model, which is a consistent result with the indoor CMR model comparison. A higher level of geometric detail creates more scatters. The CMR of the simple concrete model, however, has an even higher value than the CMR of the detailed car model, no mention about the simple model. The concrete permittivity used in the simple concrete model is much larger than any material permittivities used in the simple model, which implies a larger value of the material permittivity reflects more radio waves, and it is also verified that the influence of the material permittivity on the simulation result is not negligible.

Apparently, the channel richness of 15 GHz is richer than the one of 28 GHz, because of the higher pass loss at 28 GHz, similar to the indoor scenario. At most of the NLOS area, the channel richness distributions of these two frequencies are close to 0. In the northwest corner of the NLOS3 area, however, there are several

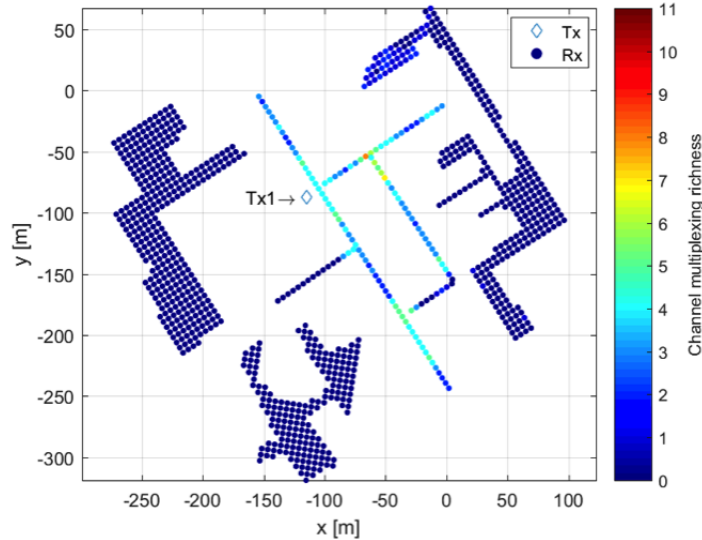


**Figure 5.3:** Outdoor 15 GHz *Simple model* CMR distribution

receivers showing a low multiplexing richness property; their CMR is up to 3 in 15 GHz and is equal to 1 in 28 GHz. At the street route area of 15 GHz, there are another three spots that the channel richness is higher or equal to 5 besides the spot around the transmitter, which are marked as C1, C2, and C3 area in figure 5.1. These three areas also appear the high richness distribution in the simple model and the simple concrete model. The largest CMR values among all occurs in the C1 area of the simple concrete model which is equal to 11. At 28 GHz, however, only the area around the transmitter and the C3 area show an obvious scattering rich property. Note that the scale bars of figure 5.1 and figure 5.4 are not in the same range, the maximum CMR value of 15 GHz is 9 and the largest CMR of 28 GHz is 4, otherwise the CMR distribution of 28 GHz is not easy to analyse.

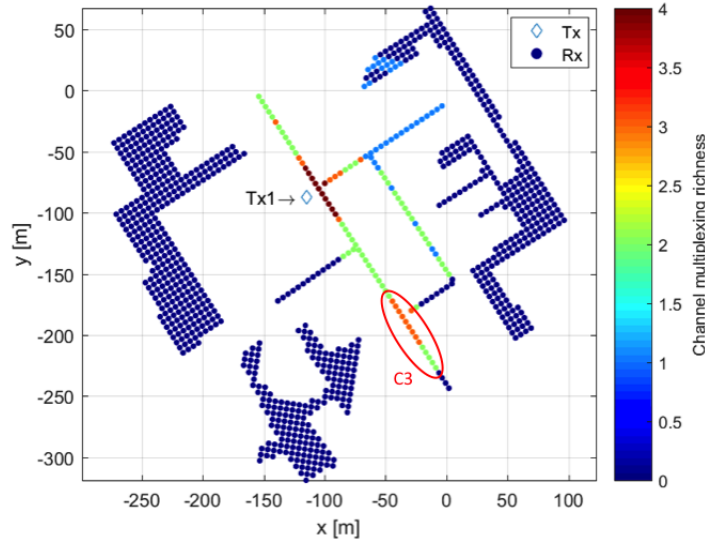


**Figure 5.4:** Outdoor 28 GHz SISO isotropic antenna element CMR distribution

## 5.2 Simulating $1 \times 32$ MISO received power

In the measurement of paper [36], the transmitter is a  $4 \times 8$  two-dimensional array with patch antenna element, and the receiver is constructed by four patch antennae arranging along the four sides of a cube. In this work, the received power of simulation is compared with the outdoor measurement in [36], to simplify the receiver structure, a monopole is used as a replacement of the cubical array with an extra 5 dB gain as the compensation for the patch element. DET is carried out in the simulation.

As the ray tracing simulation is noise free, the power of receivers with power below noise level marked as black crosses in figure 5.5 is set to the noise power. The noise power is calculated at the room temperature with 800 MHz bandwidth as equation 2.3 shows. It is equal to -105 dBm in this case. From figure 5.5, besides the street route area, there are part of receivers located in the northwest of NLOS3 region marked as P1 in a red ellipse having the received power around -58 dBm in the simulation. Since the transmitter antenna array is aligned along the ST1 route and radiates to the northeast, it is expected that the receivers in the P1 region have a large received power even without a LOS component present. The NLOS1 and NLOS2 region which are located at the back side of the transmitter array have no receivers whose power is higher than -60 dBm.

In the figure 5.7, the received power of 15 GHz DET MISO is plotted with distance of three different models. As with the empirical statistic free space model, the received power becomes lower as distance increases. By comparing with the figure 4 provided by Ericsson in [16], the simulation follows the same trend of path loss measured. Although the maximum received power of the simulation is close

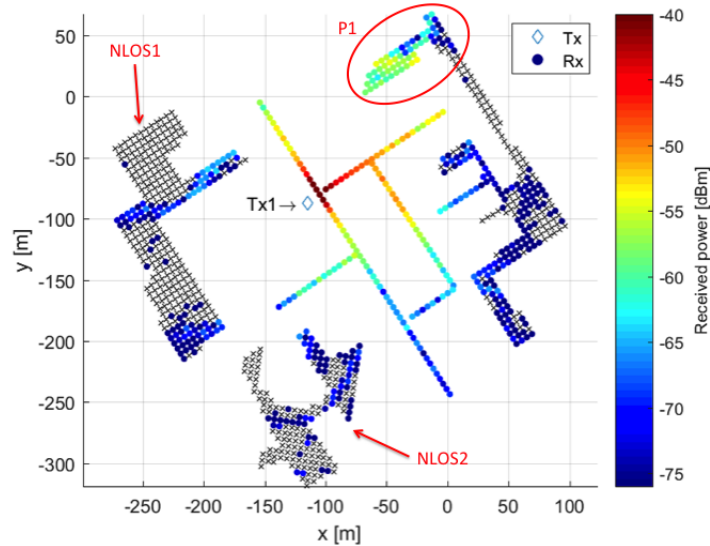
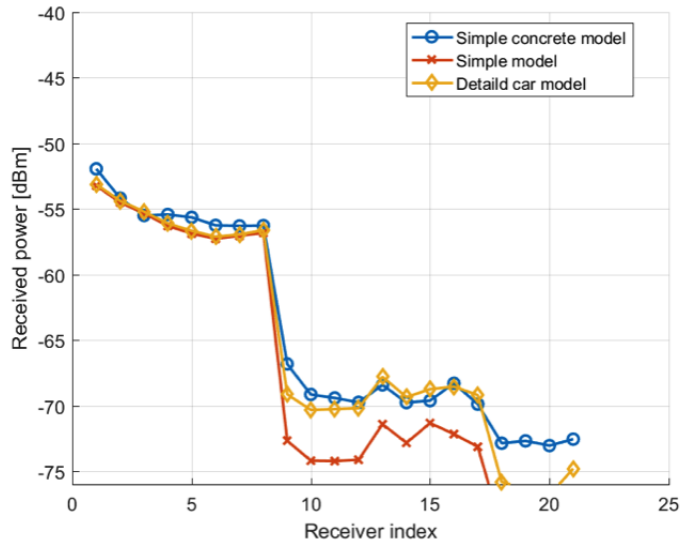


**Figure 5.5:** Outdoor 15 GHz MISO DET received power

to -35 dBm, in the received power distribution figure, the power range is -75 to -40 dBm to be consistent with the measurement. It is worthy to note that the received power variation related with the distance does not make a significant difference among three models. One slightly noticeable difference exists at the distance from 80 to 100 m that the simple model and the simple concrete model have more receivers whose power is below -67 dBm than the detailed car model. According to the phenomenon in figure 5.7, it is conjectured that the level of geometric details or the material permittivity does not have a strong impact on the received power in contrast with their influence on the CMR.

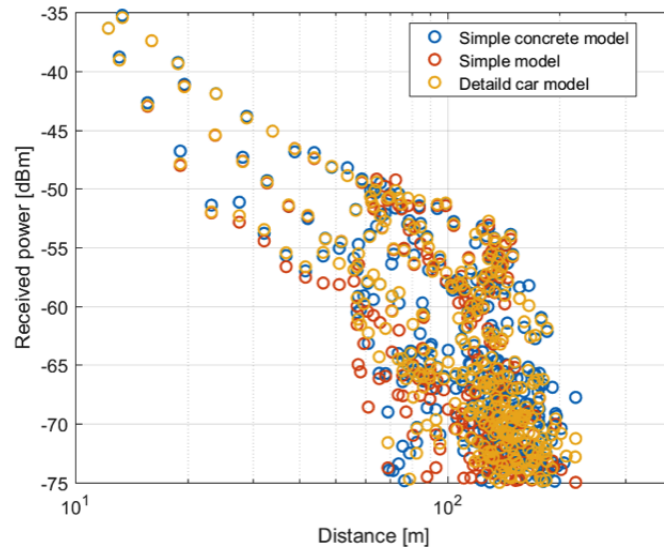
The received power difference between the measurement and simulation occurs at the range of 10 m to 20 m distance, see figure 4 in [16] of the measured received power as a function of distance. As it was described before, the transmitter height is 8.5 m, and the receiver height is 2.8 m in the simulation. At that height, when the receiver is very close to the transmitter, it is nearly below the transmitter. The monopole antenna pattern used in the simulation still have a gain at that direction, and 5 dB gain compensation is directly added to the received power regardless of direction. The cubical antenna array structure of the measurement, however, has a low gain at the vertical direction and mainly radiates at the horizontal direction. In the measurement, when the transmitter is above the receiver, a low received power is expected. Figure 5.6 shows the DET received power variation along the corner. The largest corner loss is 17 dB around in the simple model.

Figure 5.8 is the received power distribution of 28 GHz. Comparing with figure 5.5, the received power distribution of 15 GHz, they share a similar colour variation, especially in the street route region. As the noise power level is the same, -105 dBm, there are more receivers marked as black cross in figure 5.8 due



**Figure 5.6:** Outdoor 15 GHz received power corner loss comparison among three different models

to a higher free space loss. From figure 5.9, the received power of 28 GHz is 5 dB lower than the received power of 15 GHz on average. Also, it is easier to observe from figure 5.10, the received power CDF comparison of 15 and 28 GHz, that the receiver percentage whose power is -105 dBm is 49% at 15 GHz and is 62% at 28 GHz. That is, if the 28 GHz system transmitting signal using the same power of the 15 GHz system, there is another 13% receivers out of coverage.



**Figure 5.7:** Outdoor 15 GHz MISO DET received power by distance comparison among three different models

### 5.3 RMS delay spread of $8 \times 32$ MIMO channel with isotropic element

Figure 5.11 is RMS delay spread as a function of distance, in which the delay spread of 15 and 28 GHz first grow longer with the distance increases to 80 m around, and it starts to decline as the distance rises. However, some receivers which are around 140 and 175 m away have an immensely long delays. The RMS delay spread does not show an obvious dependency on the distance. In terms of frequency, the 15 GHz system has more points with long delay spread than the 28 GHz system, but the difference is not huge. It can be explained by the higher attenuation at 28 GHz compared to at 15 GHz. A plane wave through several reflections which still can be perceived by the receiver at 15 GHz may submerge into the noise level if using the 28 GHz carrier frequency. In other words, it is hard to tell the relationship of the delay spread and distance, but with a smaller carrier frequency, longer delay spreads are expected.

Figure 5.12 shows the RMS delay spread distribution of the  $8 \times 32$  isotropic MIMO channel. The black crosses in figure are receivers whose power is below the noise level since they only get few weak signals or even nothing at all. It is meaningless to calculate their delay spread, so they marked as black crosses instead. At the NLOS area, several receivers whose RMS delay is up to  $4.8 \times 10^{-7}$  s. And at 15 GHz, there are more points with this long delay. At the street route lines, the positions of four high delay spots are similar at 15 and 28 GHz.

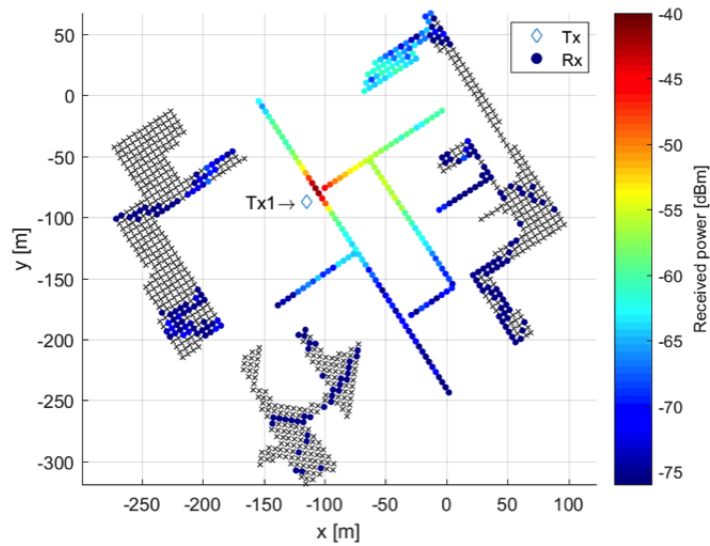


Figure 5.8: Outdoor 28 GHz MISO DET received power

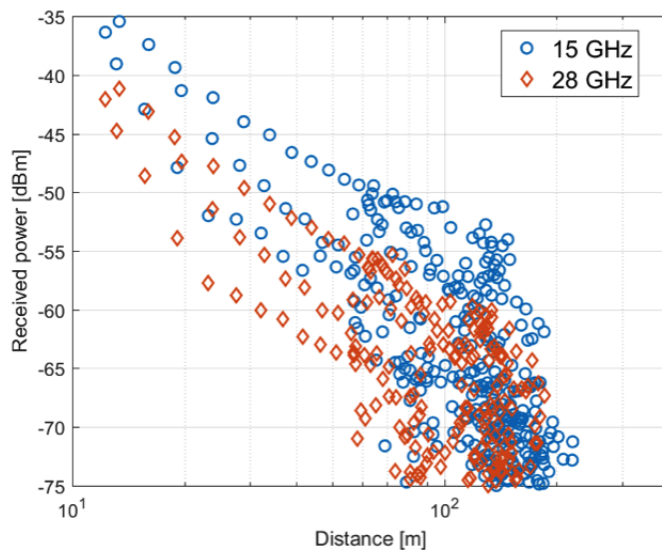
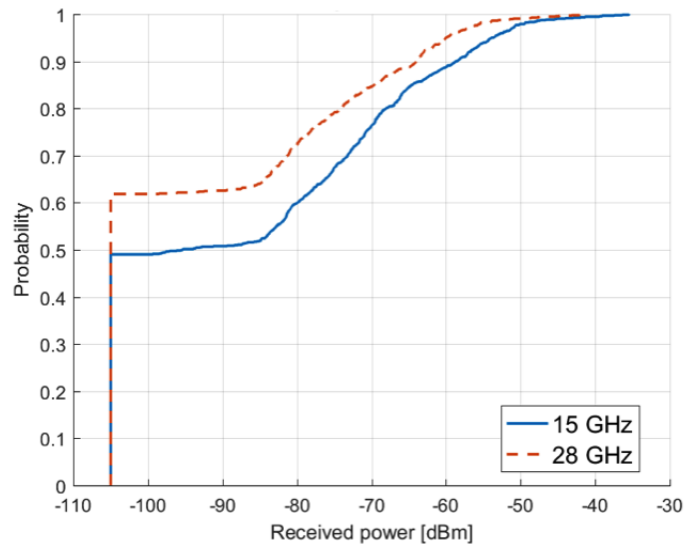
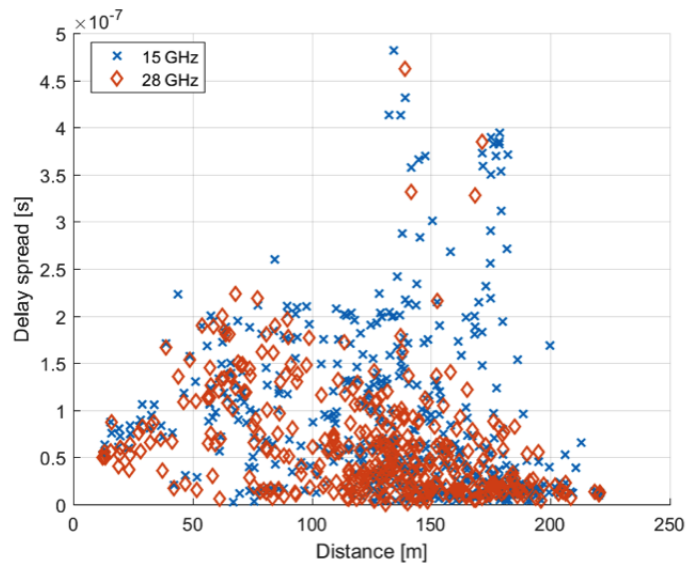


Figure 5.9: Outdoor 15 and 28 GHz MISO DET received power by distance comparison

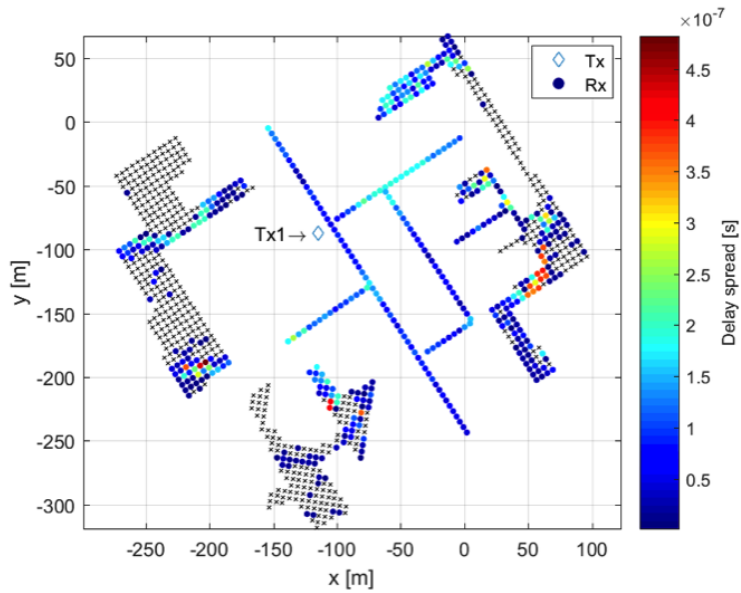




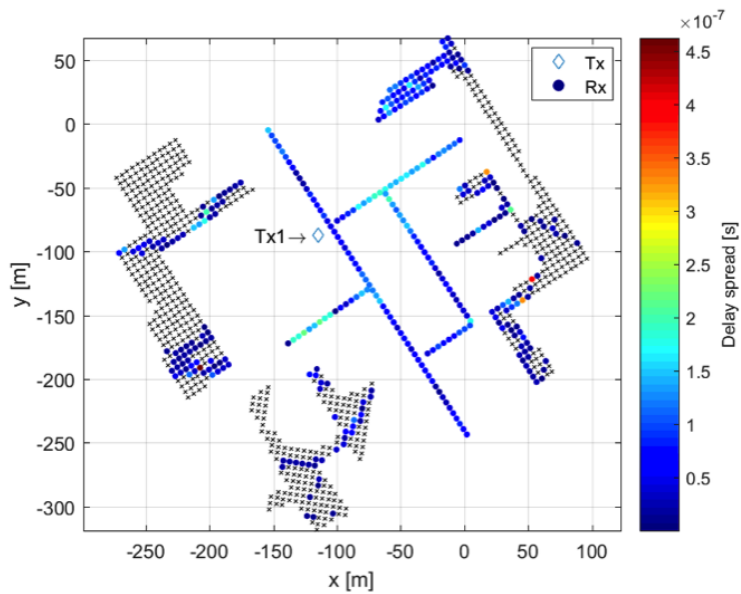
**Figure 5.10:** Outdoor 15 and 28 GHz MISO DET received power CDF comparison



**Figure 5.11:** Outdoor MIMO system isotropic antenna element delay spread with distance



(a) 15 GHz



(b) 28 GHz

**Figure 5.12:** Outdoor MIMO system patch antenna element delay spread distribution

## Outdoor $8 \times 32$ MIMO channel Capacity

The spatial multiplexing capacity distribution is presented and the capacity CDF comparison of all antenna processing techniques is given in this chapter.

### 6.1 Capacity distribution and CDF comparison

The receivers which are marked as black cross in figure 6.1 are outage points whose capacity is below the 10% outage capacity. The 10% outage capacity is calculated only considering the receivers in the street route area, since the percentage of receivers with capacity 0 bps/Hz at the NLOS area can be up to 61% at 15 GHz and up to 76% at 28 GHz, see figure 6.2 and 6.4. It is meaningless to consider the outage capacity with all receivers included, otherwise the 10% outage capacity will always be 0. The 10% outage capacity of 15 and 28 GHz of the street route area is shown in table 6.1.

**Table 6.1:** Outdoor street route area 10% outage capacity [bps/Hz]

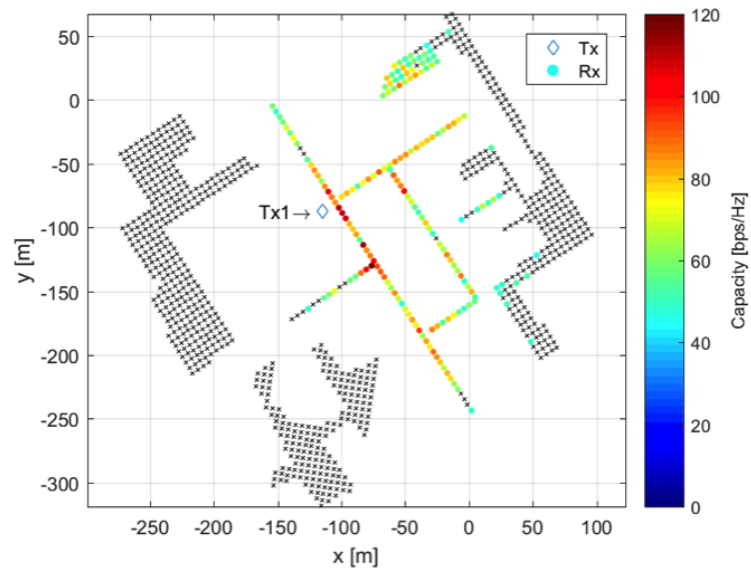
Antenna element	Isotropic		Patch	
	15 GHz	28 GHz	15 GHz	28 GHz
BF	14.34	12.94	9.75	8.53
DET	19.03	16.70	13.39	10.93
HB2	25.92	18.05	16.55	11.97
HB4	38.75	28.02	23.58	13.47
SM	45.07	33.63	28.28	17.06

Obviously, the system with isotropic antenna element has a higher capacity than the one with patch element, because the isotropic array can transmit and receive signal from both front and back side. Especially for those receivers which are located at the south of the transmitter, since, in the receiver array, the patch antenna's radiating direction is south ( see figure 3.4), only few reflected plane waves can be discerned by the main lobe while most signal is perceived by the side lobe at the back of the patch. As it is mentioned in section 3.4.2, the transmitter

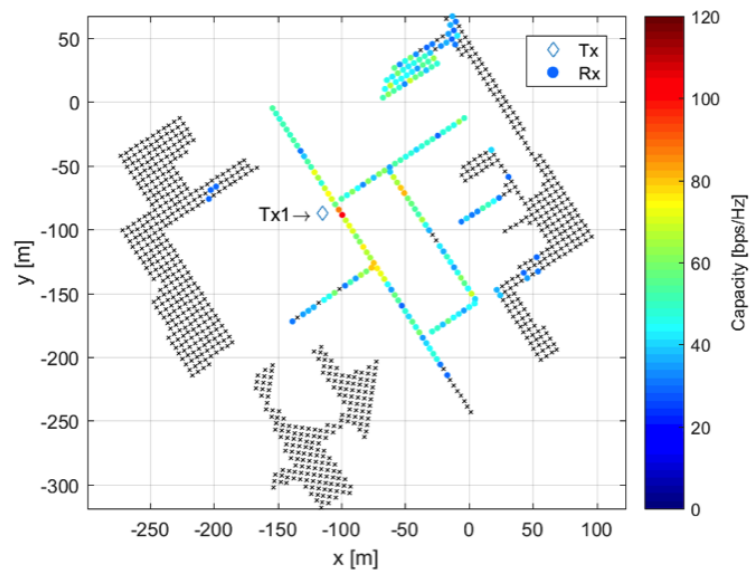
array is parallel to the ST1 route, so that patch antenna radiating direction is vertical to ST1, to the northeast. In the area NLOS1 and NLOS2, the spatial multiplexing capacities of 15 and 28 GHz are almost all 0 no matter what antenna element is utilised. At the northwest of the NLOS3 region, receivers which are located at the front side of transmitter array, the P1 region in figure 5.5, their capacities are even comparable with part of receivers at the ST area.

From figure 6.2, although the 15 GHz capacity CDFs of isotropic and patch antenna are different on values (isotropic case has a higher capacity), they share a similar trend among five different APTs: spatial multiplexing has the highest capacity while two beamforming capacity are the lowest. In the 15 GHz capacity CDF comparison of the NLOS area, there is 61% receivers detecting no valid signals if the patch antenna is utilised, and the percentage is 57% if the isotropic antenna is utilised.

Figure 6.3 is the spatial multiplexing capacity distribution of 28 GHz. Its capacity distribution is similar with the 15 GHz capacity distribution but apparently shows a lower capacity. Figure 6.4 is the capacity CDF comparison of two areas. At the ST area, the spatial multiplexing still provides the largest capacity. At the NLOS area, the probability of 0 bps/Hz capacity is up to 72% with isotropic antenna and is up to 76% with patch antenna, which is much larger than the percentage of 15 GHz.

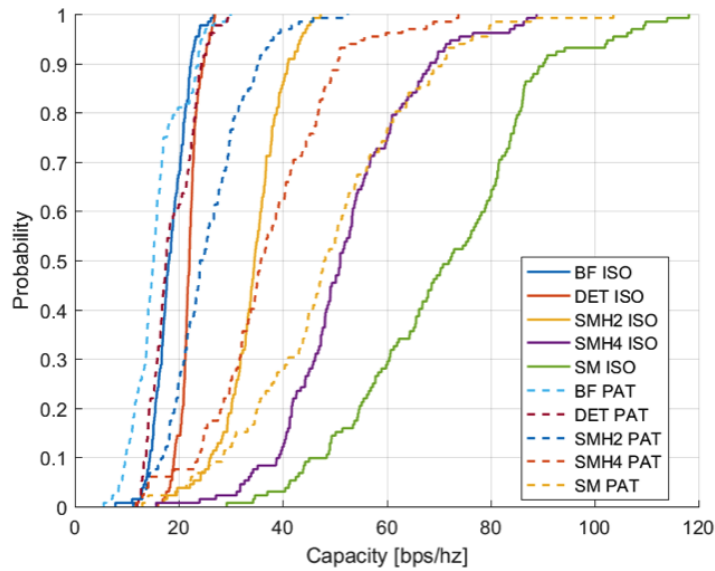


(a) Isotropic

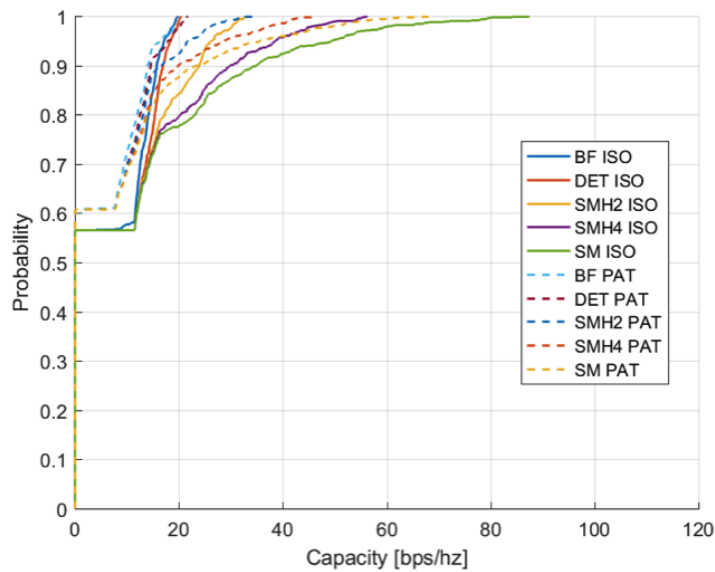


(b) Patch

**Figure 6.1:** Outdoor 15 GHz spatial multiplexing capacity distribution

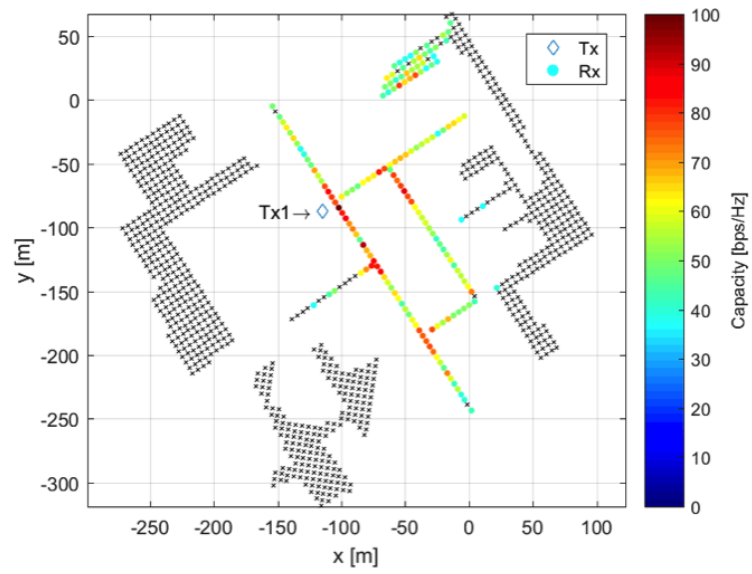


(a) Street route area

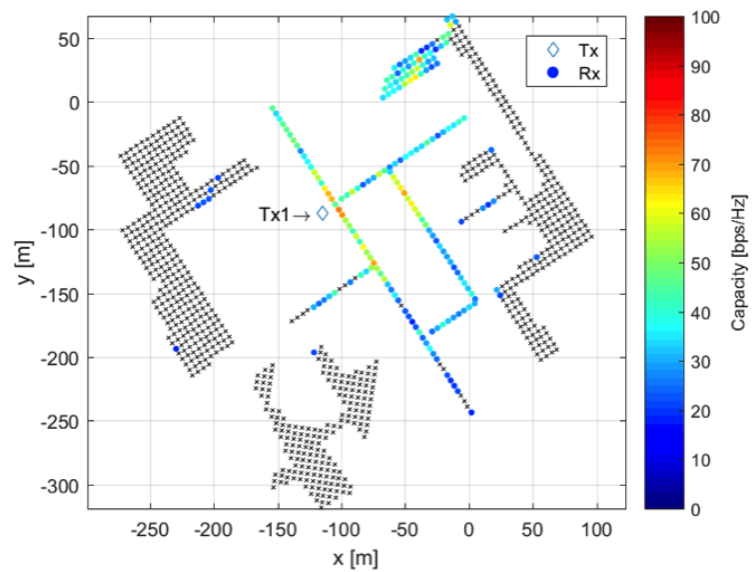


(b) NLOS area

**Figure 6.2:** Outdoor 15 GHz spatial multiplexing capacity CDF comparison

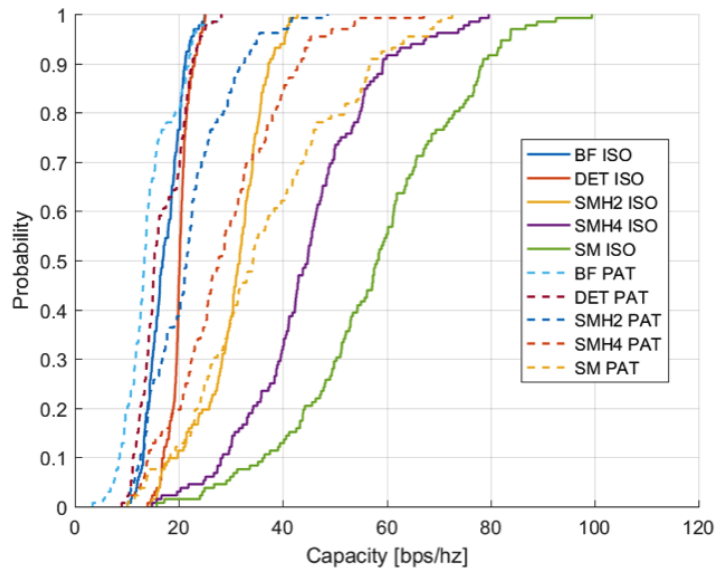


(a) Isotropic

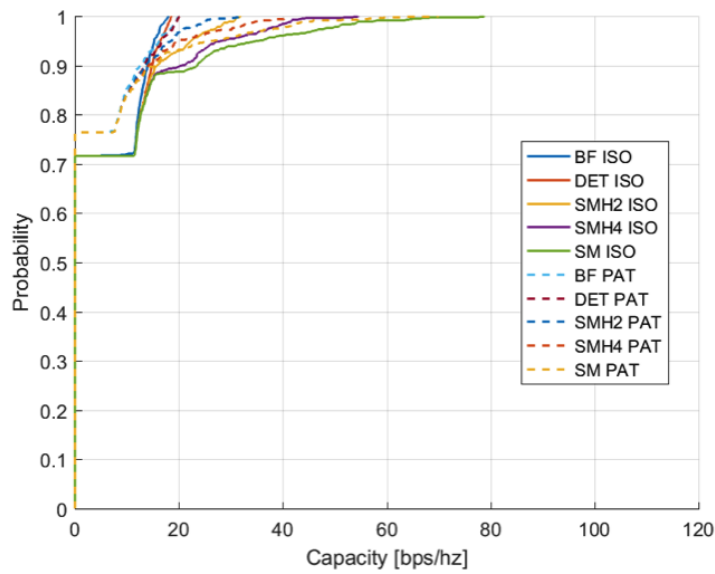


(b) Patch

**Figure 6.3:** Outdoor 28 GHz spatial multiplexing capacity distribution



(a) Street route area



(b) NLOS area

**Figure 6.4:** Outdoor 28 GHz spatial multiplexing capacity CDF comparison



## 6.2 Capacity of rotating receiver

In the outdoor scenario, three receivers Rx19, 44, and 82 are chosen to calculate their capacity changes when the antenna array rotates in parallel to the ground. This case is created in order to emulate a user that is facing an arbitrary direction. Figure 6.5 shows the locations of these three chosen receivers. Rx19 is the closest one to transmitter among all receivers at the ST area, and thus it has a strong LOS component.

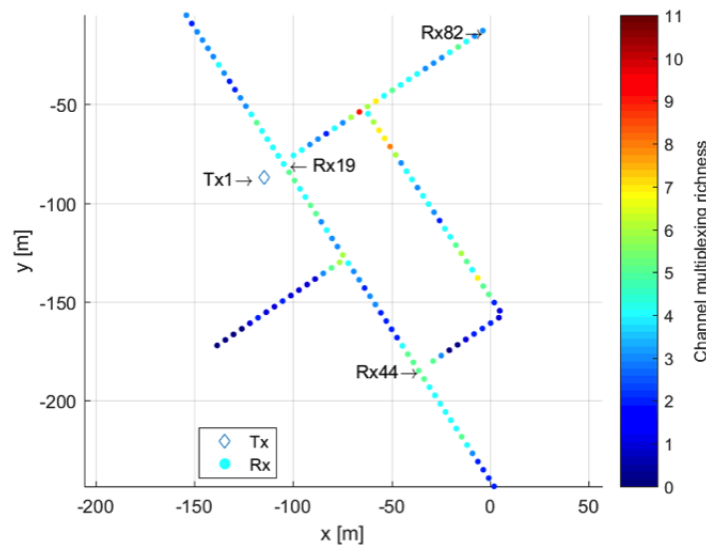
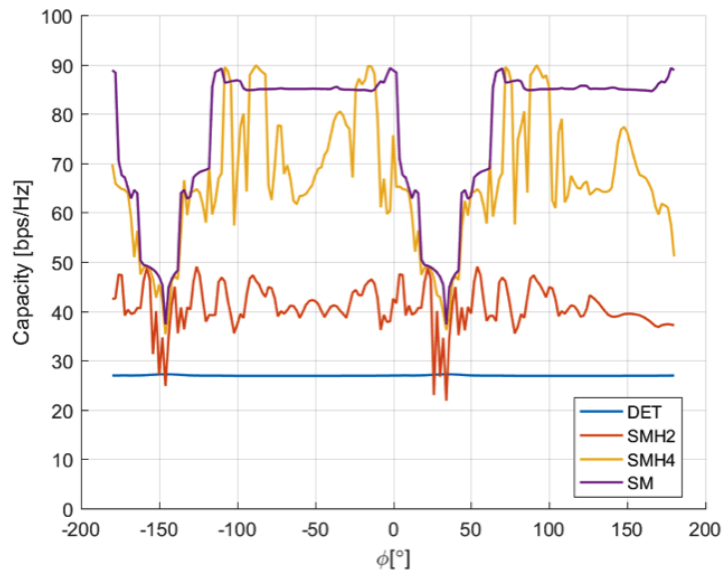


**Figure 6.5:** Outdoor receiver positions of varying orientations

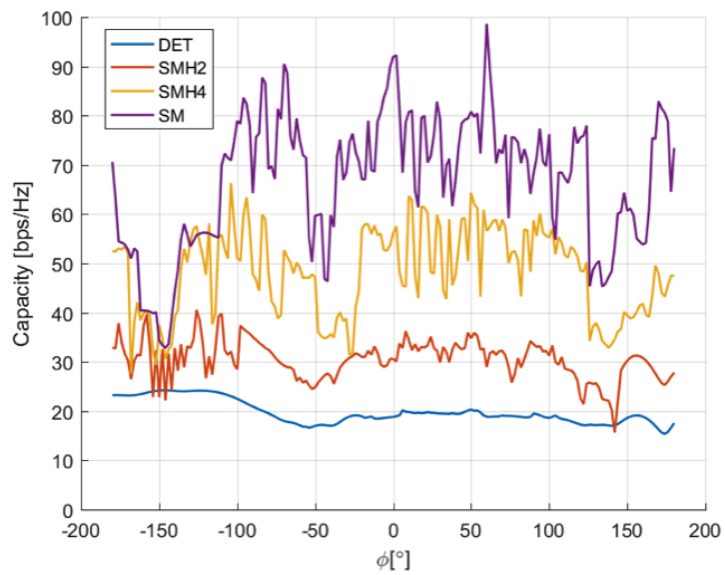
Figure 6.6 is the rotating capacity of Rx19 with the isotropic and patch element. The  $\phi$  axis is the radiating direction of the linear array and is consistent with the azimuth plane coordinate. For example, when the  $\phi$  angle is  $0^\circ$ , the receiver linear array is aligned north-south direction; And if the patch antenna element is applied, its radiating direction is east. So that the default receiver array alignment which is along the  $\hat{x}$  direction used in all the outdoor models before is when  $\phi$  angle is equal to  $-90^\circ$ .

The rotating capacity curve of the isotropic antenna in figure 6.6a shows an obvious repeated pattern in which the period starts from  $-145^\circ$  to  $35^\circ$ . Capacities of spatial multiplexing and hybrid beamforming have a deep drop when receiver array rotates at these two direction. The capacity of DET is steady in figure 6.6a. Figure 6.6b shows the rotating capacity when patch antenna is applied. As Rx19 is very close to Tx, when the patch array rotates to face the front side of each other, the channel is under the influence of a strong LOS component. According to the *Angle of Arrival* (AOA) in figure 6.7b, the strong LOS component comes from  $-145^\circ$   $\phi$  angle. The capacity of DET has an improvement around  $-145^\circ$  direction, due to a higher SNR. For the capacity of spatial multiplexing and hybrid beamforming, however, a deep drop exits since a strong LOS component makes the channel rank-

deficient [25]. Even in the drop of the spatial multiplexing curve, its capacity is still larger than or equal to the capacity of the DET method.

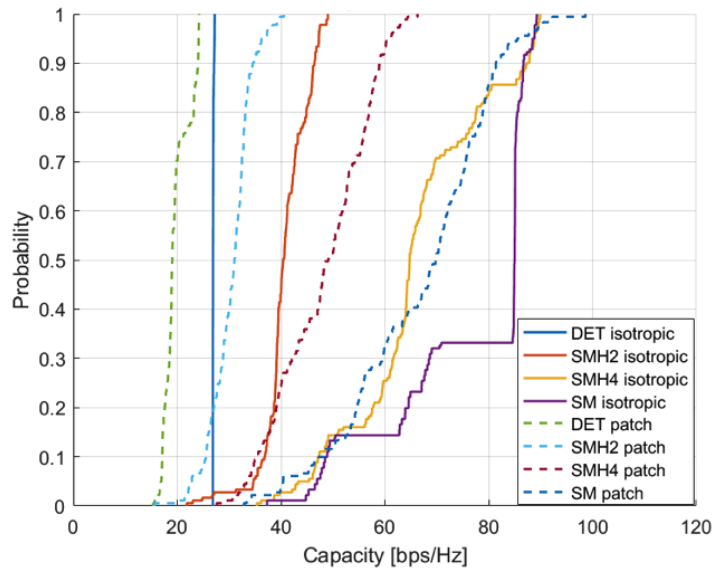


(a) Isotropic

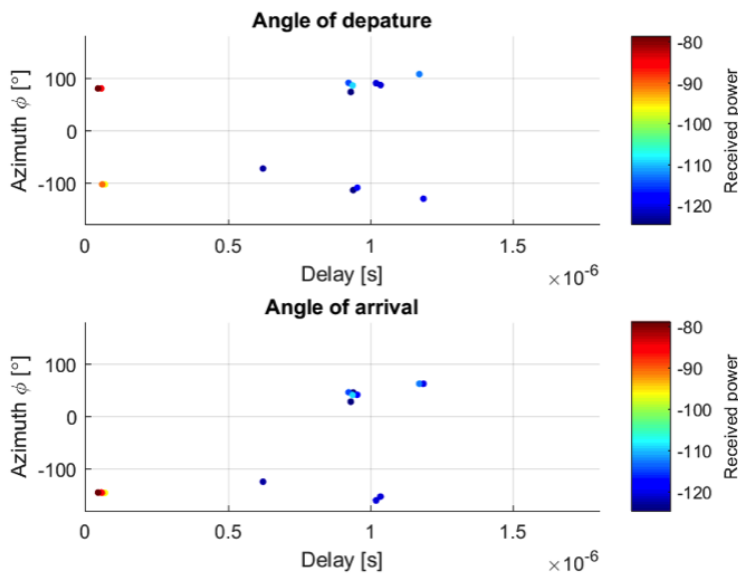


(b) Patch

**Figure 6.6:** Outdoor 15 GHz Rx19 rotating capacity



(a) Rotating capacity CDF comparison



(b) AOA and AOD

**Figure 6.7:** Outdoor 15 GHz Rx19 rotating capacity CDF and angular spread

This thesis has investigated the utilisation of the ray-tracing simulation in the mm-Wave propagation performance, and discussed the capacity improvement capabilities of beamforming, spatial multiplexing, and hybrid beamforming. In the indoor scenario, the AOD and PDP based on the ray-tracing simulation show a fair match with the results from the measurement. The synthesised antenna array method makes the simulation data of the isotropic SISO channel available to combine with different antenna patterns and array configurations. Also, in the outdoor scenario, the 15 GHz received power from simulation is consistent with the signal strength in the measurement.

A new variable channel multiplexing richness is defined in this work; it is a simple way to find out the simulating result differences among models. By comparing the CMR and received power of different simulation models, simple or detailed structures, the material permittivity and the level of geometric details have notable influence on the ray-tracing simulation. That is, to make the ray-tracing simulation as accurate as possible, the virtual environment should include detailed objects; objects involved should be set the correct material permittivity.

According to the outdoor received power distribution, it is concluded that the communication system using 15 GHz has a larger coverage than using 28 GHz; it is expected because of higher free space path loss at higher frequency band. The RMS delay spread does not show an apparent dependency on the distance, but it is expected to have a shorter delay spread with a higher carrier frequency. In the different antenna processing technique cases, the spatial multiplexing shows the highest capacity performance; and it is the optimal solution in terms of the capacity.

## 7.1 Future work

In this project, the  $8 \times 32$  MIMO channel capacity is calculated under the single user condition. In reality, it is common that the base station needs to provide the throughput to more than one receiver at the same time. It is interesting to see the channel capacity performance of these five antenna processing techniques in the multiple user case, and compare the difference with the results presented in this work.

Another important factor which influences the channel property is the shad-

owing effect caused by users or moving objects, such as cars and trucks. The next step of exploring the indoor shadowing effect due to users is adding several phantoms imitating human body and comparing the simulation result with the indoor case where no phantoms are present.

Last, in this research, since only one transmitter is simulated, it is limited to implement different base station techniques. For example, two base stations can work together, using coordinated multi-point techniques.

---

## References

---

- [1] Tomislav Stimac. Definition of frequency bands. <http://www.vlf.it/frequency/bands.html>. Accessed: 2016-02-02.
- [2] Theodore S Rappaport, Shu Sun, Rimma Mayzus, Hang Zhao, Yaniv Azar, Kevin Wang, George N Wong, Jocelyn K Schulz, Mathew Samimi, and Felix Gutierrez. Millimeter wave mobile communications for 5G cellular: It will work! *IEEE access*, 1:335–349, 2013.
- [3] Lili Wei, Rose Qingyang Hu, Yi Qian, and Geng Wu. Key elements to enable millimeter wave communications for 5G wireless systems. *IEEE Wireless Communications*, 21(6):136–143, 2014.
- [4] Fredrik Rusek, Daniel Persson, Buon Kiong Lau, Erik G Larsson, Thomas L Marzetta, Ove Edfors, and Fredrik Tufvesson. Scaling up MIMO: Opportunities and challenges with very large arrays. *IEEE Signal Processing Magazine*, 30(1):40–60, 2013.
- [5] Juyul Lee, Jinyi Liang, Jae-Joon Park, and Myung-Don Kim. Directional path loss characteristics of large indoor environments with 28 GHz measurements. In *Personal, Indoor, and Mobile Radio Communications (PIMRC), 2015 IEEE 26th Annual International Symposium on*, pages 2204–2208, Aug 2015.
- [6] Mingyang Lei, Jianhua Zhang, Tian Lei, and Detao Du. 28-GHz indoor channel measurements and analysis of propagation characteristics. In *Personal, Indoor, and Mobile Radio Communication (PIMRC), 2014 IEEE 25th Annual International Symposium on*, pages 208–212, Sept 2014.
- [7] Yaniv Azar, George N Wong, Kevin Wang, Rimma Mayzus, Jocelyn K Schulz, Hang Zhao, Felix Gutierrez, DuckDong Hwang, and Theodore S Rappaport. 28 GHz propagation measurements for outdoor cellular communications using steerable beam antennas in New York city. In *2013 IEEE International Conference on Communications (ICC)*, pages 5143–5147. IEEE, 2013.
- [8] Jianwu Dou, Nan Zhang, Li Tian, Xiaoyi Yang, Xi Yuan, Suping Mei, and Haiming Wang. Propagation channel comparison between 23.5 and 45 GHz in conference scenario. *Chin. J. Eng.*

- [9] T Imai, K Kitao, N Tran, N Omaki, Y Okumura, M Sasaki, and W Yamada. Development of high frequency band over 6 GHz for 5G mobile communication systems. In *2015 9th European Conference on Antennas and Propagation (EuCAP)*, pages 1–4. IEEE, 2015.
- [10] Xin Zhou, Zhangdui Zhong, Bei Zhang, Ruisi He, Ke Guan, Qi Wang, and David Matolak. Experimental characterization and correlation analysis of indoor channels at 15 GHz. *International Journal of Antennas and Propagation*, 2015, 2015.
- [11] Pawel Kulakowski and Wieslaw Ludwin. Performance analysis of multiple-input multiple-output system for wireless network in an office room. *AEU-International Journal of Electronics and Communications*, 60(3):240–243, 2006.
- [12] Sooyoung Hur, Sangkyu Baek, ByungChul Kim, JeongHo Park, Andreas F Molisch, Katsuyuki Haneda, and Michael Peter. 28 GHz channel modeling using 3D ray-tracing in urban environments. In *Antennas and Propagation (EuCAP), 2015 9th European Conference on*, pages 1–5. IEEE, 2015.
- [13] Bolun Guo, Yong Wu, Meiyang Yang, and Jian Li. 28GHz millimeter wave propagation models based on ray-tracing in urban scenario. In *Personal, Indoor, and Mobile Radio Communications (PIMRC), 2015 IEEE 26th Annual International Symposium on*, pages 2209–2213. IEEE, 2015.
- [14] Eric Torkildson, Colin Sheldon, Upamanyu Madhow, and Mark Rodwell. Millimeter-wave spatial multiplexing in an indoor environment. In *2009 IEEE Globecom Workshops*, pages 1–6. IEEE, 2009.
- [15] Katsuyuki Haneda, Carl Gustafson, and Shurjeel Wyne. 60 GHz spatial radio transmission: multiplexing or beamforming? *IEEE Transactions on Antennas and Propagation*, 61(11):5735–5743, 2013.
- [16] Peter Ökvist, Henrik Asplund, Arne Simonsson, Björn Halvarsson, Jonas Medbo, and Nima Seifi. 15 GHz propagation properties assessed with 5G radio access prototype. In *Personal, Indoor, and Mobile Radio Communications (PIMRC), 2015 IEEE 26th Annual International Symposium on*, pages 2220–2224. IEEE, 2015.
- [17] Claude Shannon. A mathematical theory of communication. *ACM SIGMOBILE Mobile Computing and Communications Review*, 5(1):3–55, 2001.
- [18] Emre Telatar. Capacity of multi-antenna gaussian channels. *European transactions on telecommunications*, 10(6):585–595, 1999.
- [19] Remcom, Inc, 315 S. Allen St., Suite 416 State College, PA 16801. *Wireless InSite 2.8.0 Reference Manual*, October 2015.
- [20] Andreas F. Molisch. *Wireless communications: second edition*. John Wiley & Sons, 2011.
- [21] Andrea Goldsmith. *Wireless communications*. Cambridge university press, 2005.



- [22] Massimiliano Comisso. Beamforming techniques for wireless communications in low-rank channels: analytical models and synthesis algorithms. 2008.
- [23] Yu-Shin Cheng and Chih-Hsuan Chen. A novel 3D beamforming scheme for LTE-Advanced system. In *Network Operations and Management Symposium (APNOMS), 2014 16th Asia-Pacific*, pages 1–6. IEEE, 2014.
- [24] Shurjeel Wyne, Katsuyuki Haneda, Sylvain Ranvier, Fredrik Tufvesson, and Andreas F Molisch. Beamforming effects on measured mm-wave channel characteristics. *Wireless Communications, IEEE Transactions on*, 10(11):3553–3559, 2011.
- [25] Arogyaswami Paulraj, Rohit Nabar, and Dhananjay Gore. *Introduction to space-time wireless communications*. Cambridge university press, 2003.
- [26] Thomas M Cover and Joy A Thomas. *Elements of information theory*. John Wiley & Sons, 2012.
- [27] Chen-Nee Chuah, Joseph M Kahn, and David Tse. Capacity of multi-antenna array systems in indoor wireless environment. In *Global Telecommunications Conference, 1998. GLOBECOM 1998. The Bridge to Global Integration. IEEE*, volume 4, pages 1894–1899. IEEE, 1998.
- [28] Shunsuke Fujio et.al. Robust beamforming method for SDMA with interleaved subarray hybrid beamforming. *IEEE PIMRC 2016*, Sept 2016.
- [29] Joseph Schuster and Raymond Luebbers. Comparison of site-specific radio propagation path loss predictions to measurements in an urban area. In *Antennas and Propagation Society International Symposium, 1996. AP-S. Digest*, volume 2, pages 1210–1213. IEEE, 1996.
- [30] J Schuster and R Luebbers. Hybrid sbr/gtd radio propagation model for site specific predictions in an urban environment. *12th Annual Rev. of Progress in Applied Computational Electromagnetics*, 1:8492, 1996.
- [31] IEEE standard definitions of terms for radio wave propagation. *ANSI/IEEE Std 211-1977*, Aug 1977.
- [32] Sooyoung Hur, Sangkyu Baek, Byungchul Kim, Youngbin Chang, Andreas F Molisch, Theodore S Rappaport, Katsuyuki Haneda, and Jeongho Park. Proposal on millimeter-wave channel modeling for 5G cellular system. *IEEE Journal of Selected Topics in Signal Processing*, 10(3):454–469, 2016.
- [33] Stephen G Larew, Timothy A Thomas, Mark Cudak, and Amitava Ghosh. Air interface design and ray tracing study for 5G millimeter wave communications. In *2013 IEEE Globecom Workshops (GC Wkshps)*, pages 117–122. IEEE, 2013.
- [34] Iman Vakili. *Time-Domain Antenna and Scattering Analysis for Micro- and Millimeter-Wave Applications*. PhD thesis, Lund University, 2015.
- [35] ITU-R. P.2040 : Effects of building materials and structures on radio wave propagation above about 100 MHz. Technical report, ITU, 2015.

- 
- [36] Stefan Parkvall, Johan Furuskog, Yoshihisa Kishiyama, Atsushi Harada, Takehiro Nakamura, Peter Naucler, and Bjorn Halvarsson. 5G wireless access-trial concept and results. In *2015 IEEE Global Communications Conference (GLOBECOM)*, pages 1–6. IEEE, 2015.

---

Appendix **A**

Appendix

---

A.1 Indoor scenario

A.1.1 Indoor MISO 15 GHz

PDP comparison between measurement and simulation

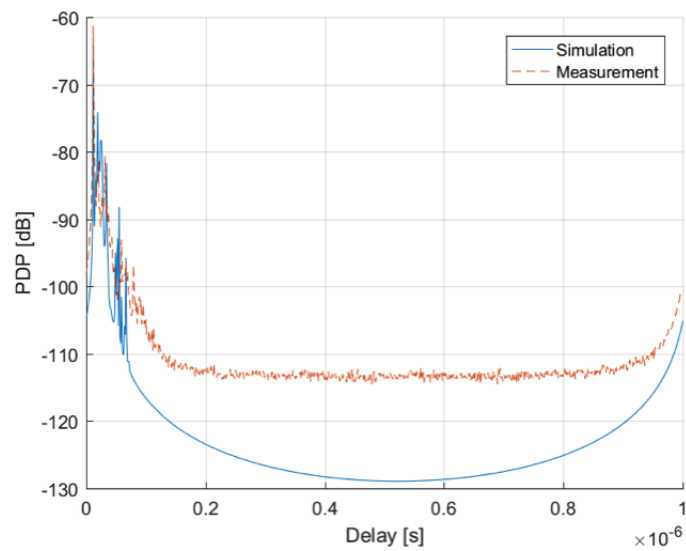


**Figure A.1:** Indoor 15 GHz MISO PDP comparison Rx1

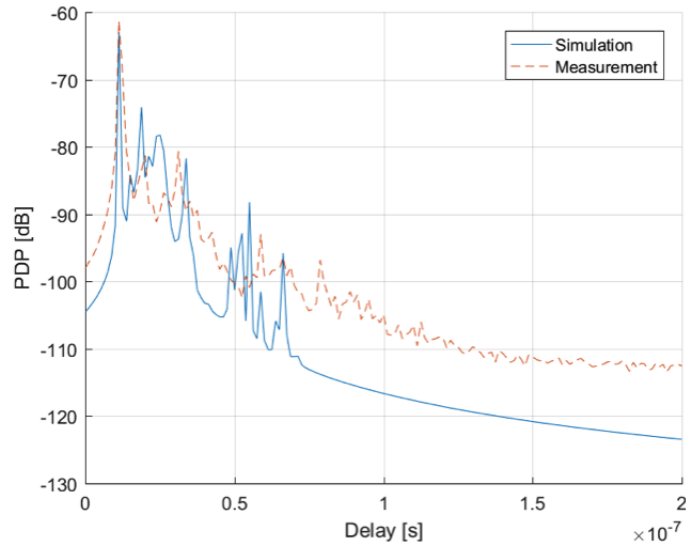


**Figure A.2:** Indoor 15 GHz MISO PDP comparison Rx1 magnified

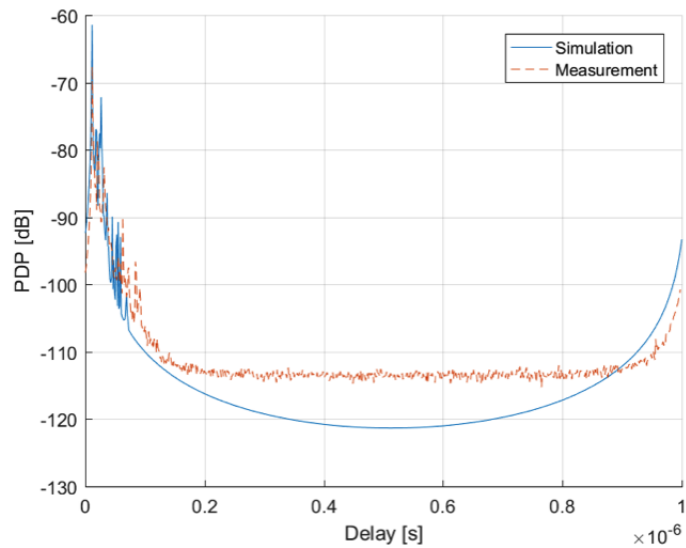


**Figure A.3:** Indoor 15 GHz MISO PDP comparison Rx2

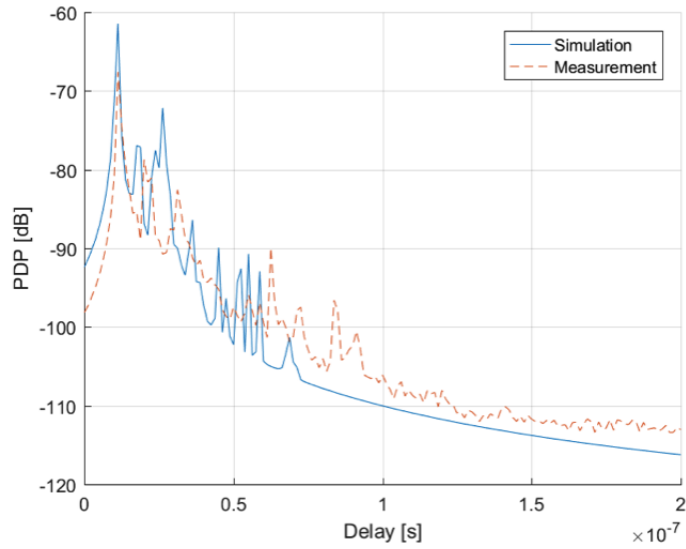


Figure A.4: Indoor 15 GHz MISO PDP comparison Rx2 magnified

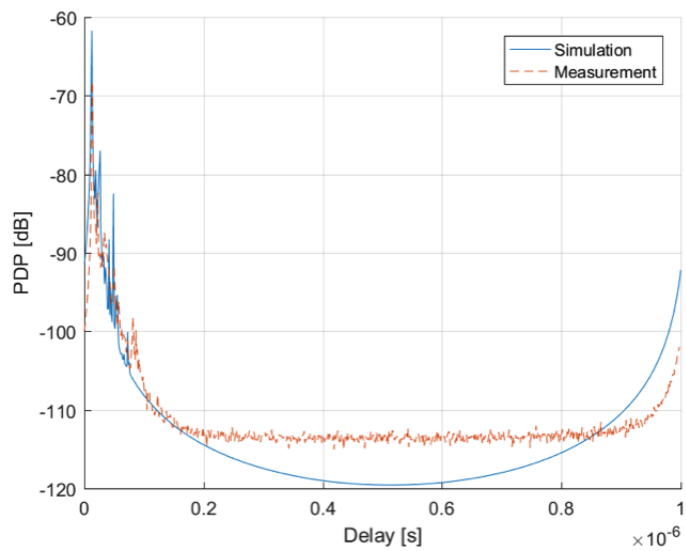
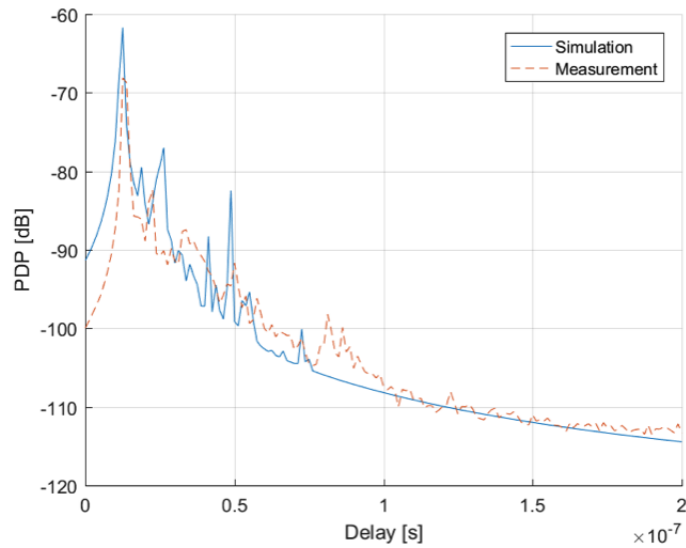
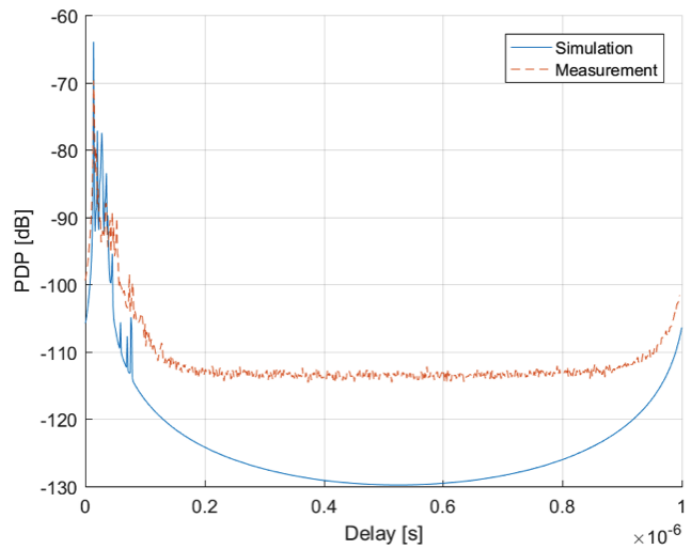


Figure A.5: Indoor 15 GHz MISO PDP comparison Rx3



**Figure A.6:** Indoor 15 GHz MISO PDP comparison Rx3 magnified



**Figure A.7:** Indoor 15 GHz MISO PDP comparison Rx4

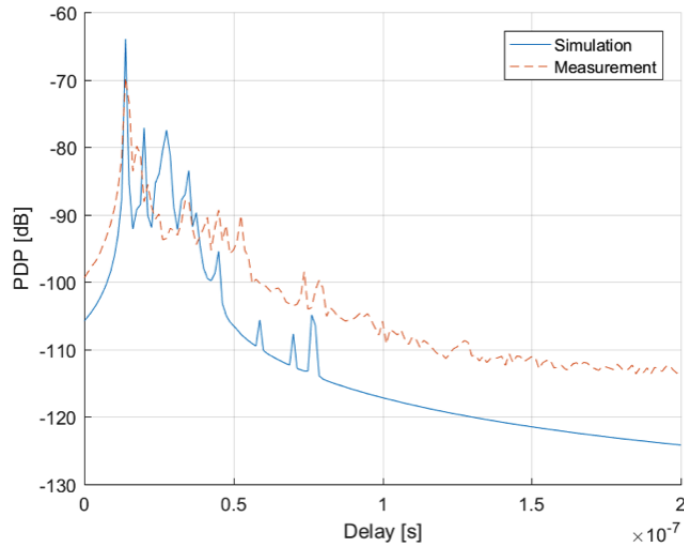


Figure A.8: Indoor 15 GHz MISO PDP comparison Rx4 magnified

Angular spread

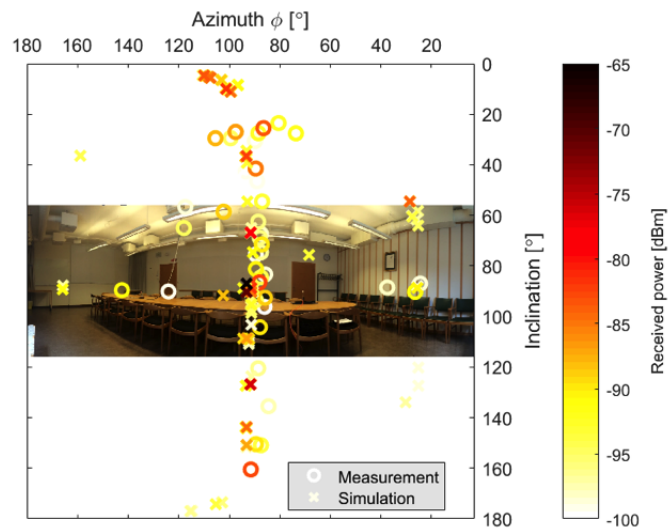
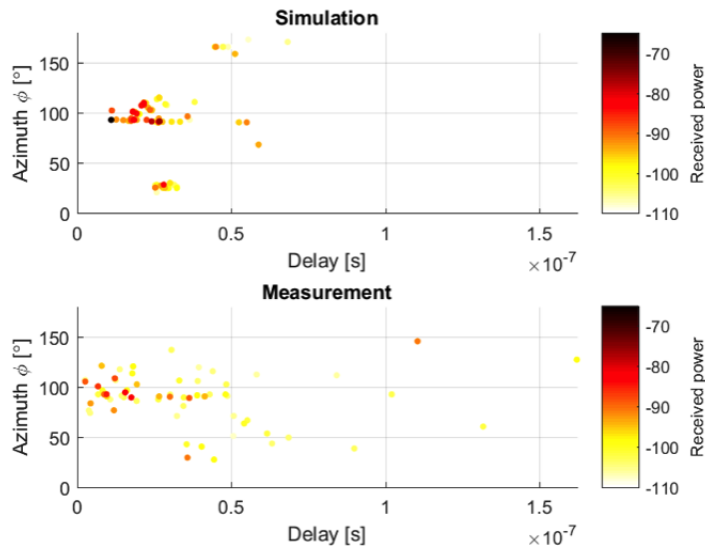
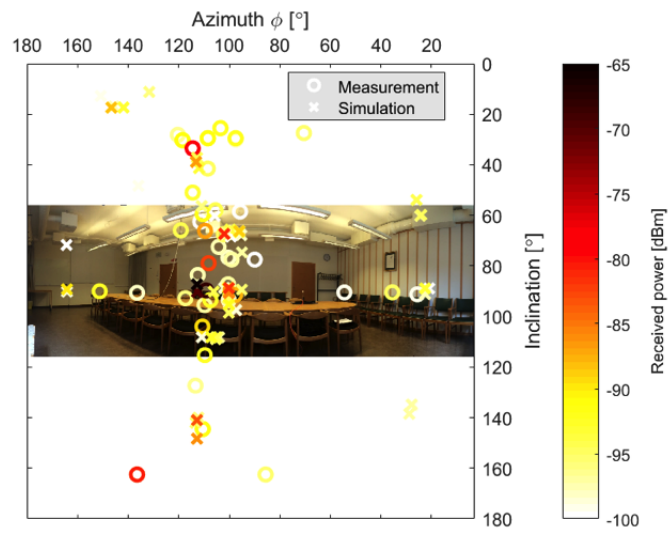


Figure A.9: Indoor 15 GHz AOD Rx2 view from transmitter



**Figure A.10:** Indoor 15 GHz AOD Rx2 angular spread with delay time



**Figure A.11:** Indoor 15 GHz AOD Rx3 view from transmitter



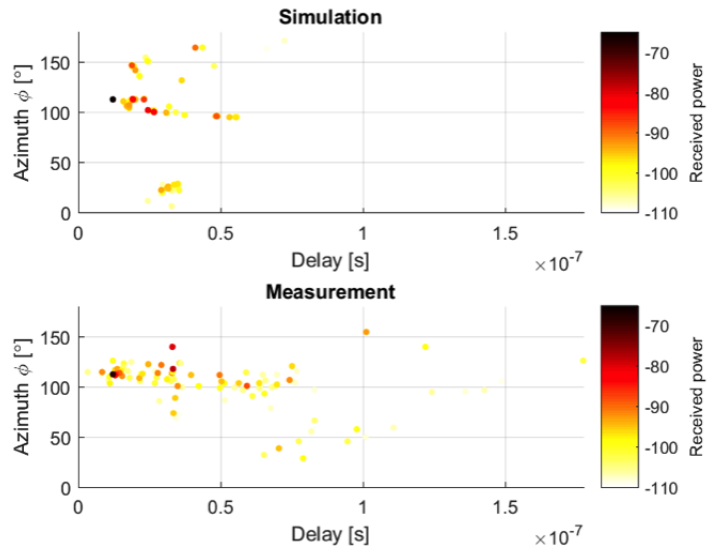


**Figure A.12:** Indoor 15 GHz AOD Rx3 angular spread with delay time

## A.2 Outdoor scenario

### A.2.1 Capacity of 15 GHz with isotropic element

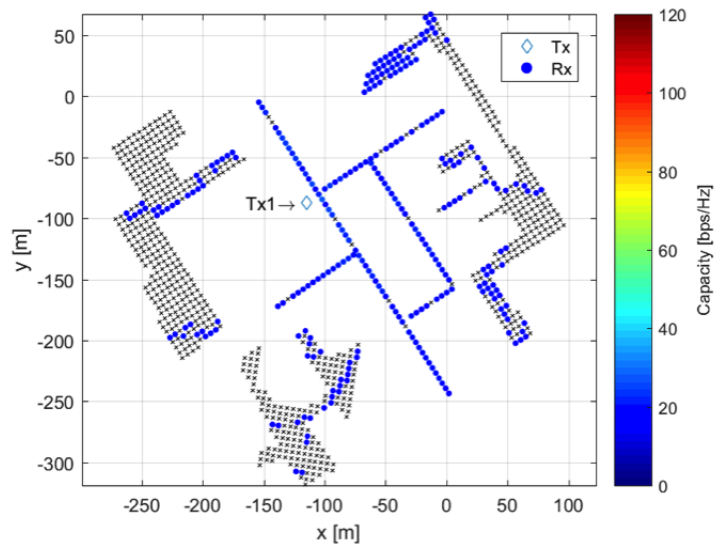


**Figure A.14:** Outdoor 15 GHz isotropic BF capacity

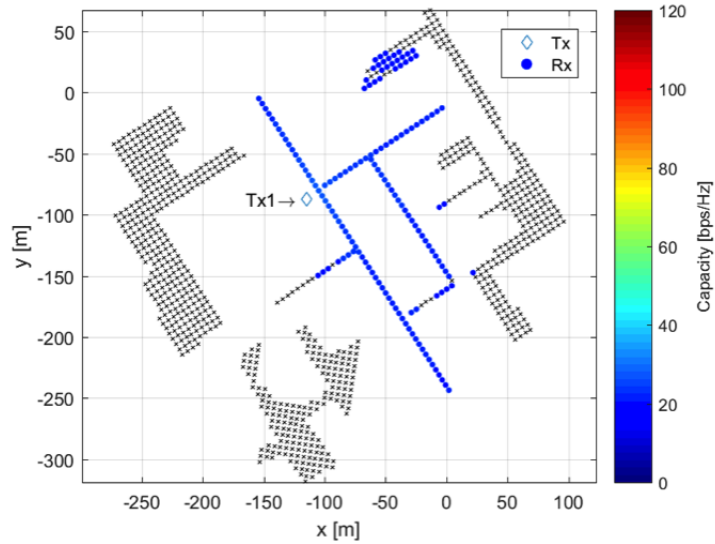


Figure A.13: Outdoor 15 GHz isotropic DET capacity

### A.2.2 Capacity of 15 GHz with patch element

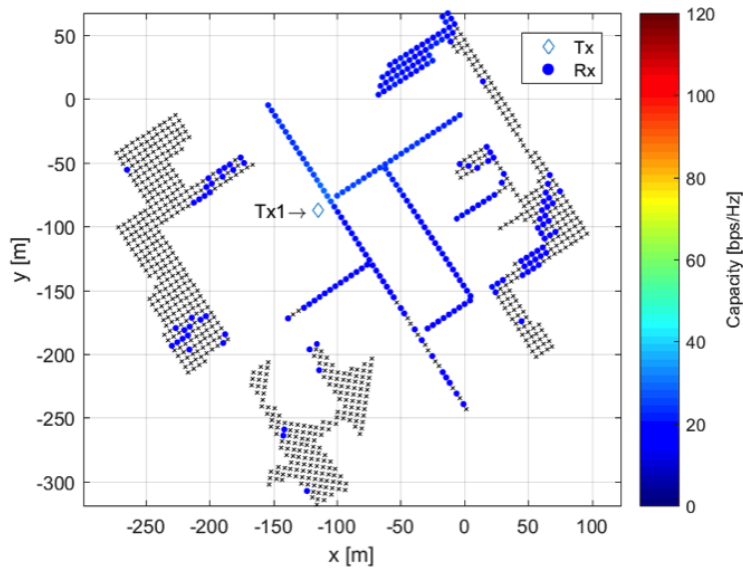
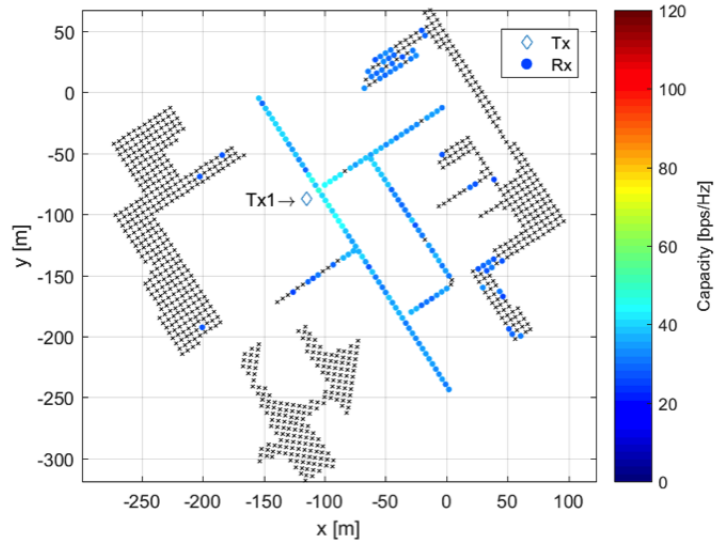
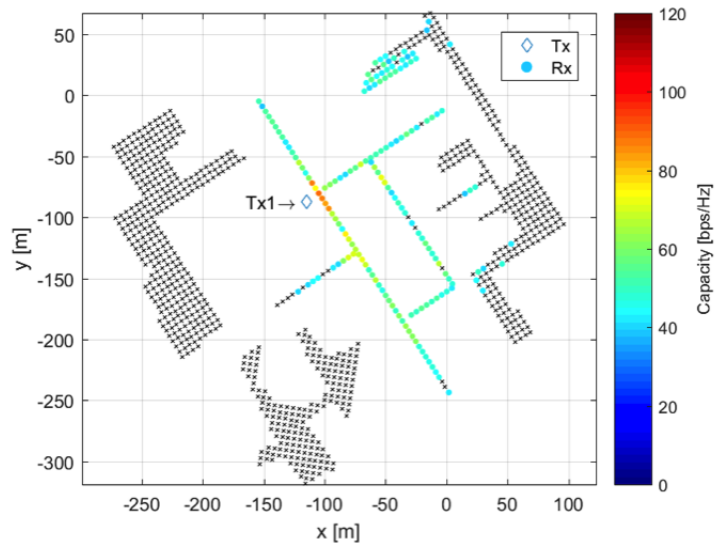


Figure A.17: Outdoor 15 GHz patch DET capacity



**Figure A.15:** Outdoor 15 GHz isotropic SMH2 capacity



**Figure A.16:** Outdoor 15 GHz isotropic SMH4 capacity

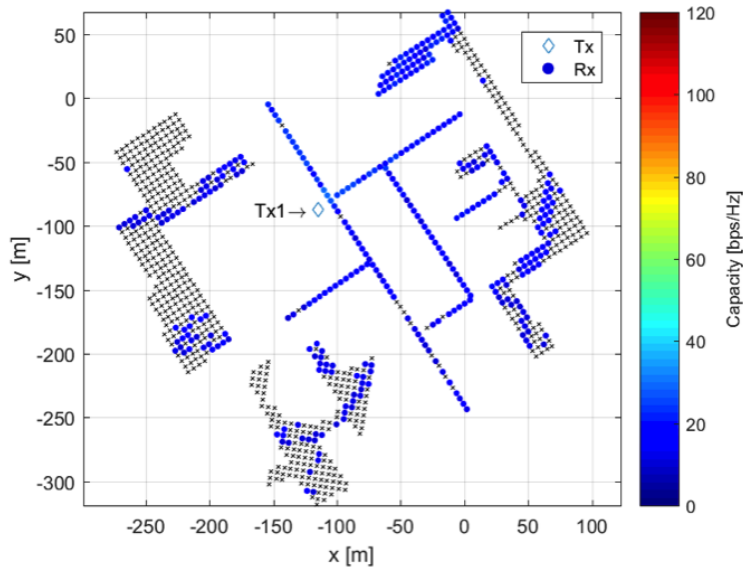


Figure A.18: Outdoor 15 GHz patch BF capacity

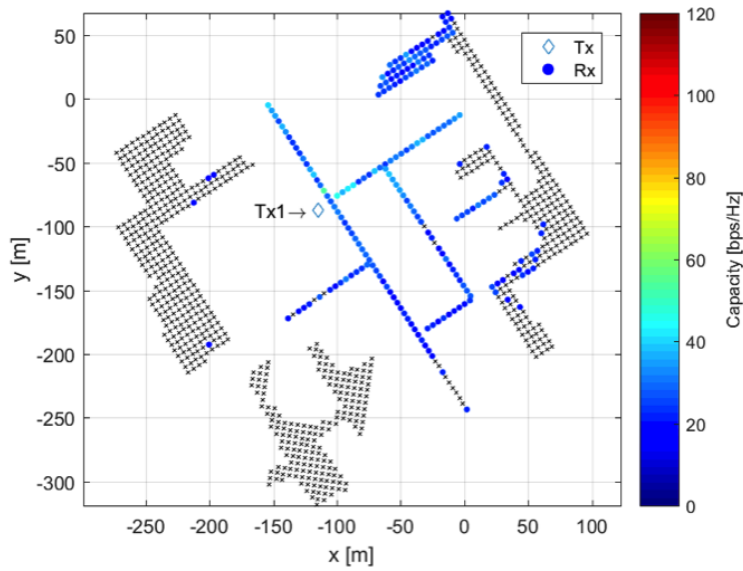


Figure A.19: Outdoor 15 GHz patch SMH2 capacity

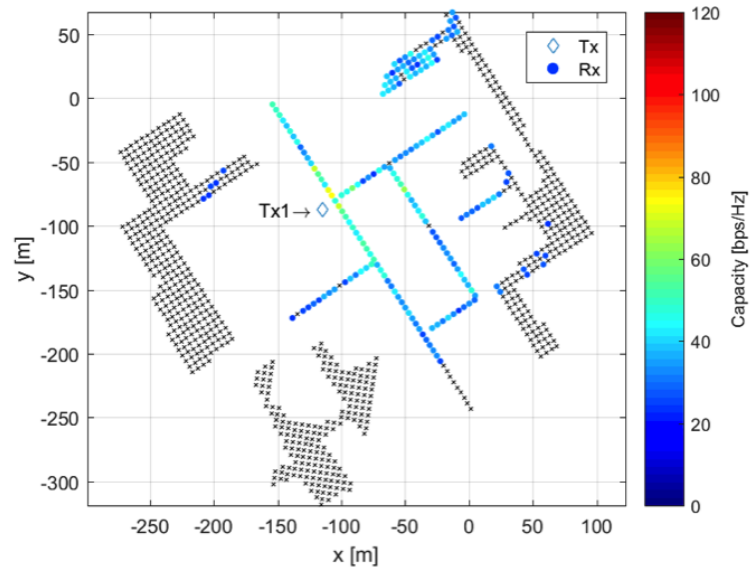


Figure A.20: Outdoor 15 GHz patch SMH4 capacity

### A.2.3 Capacity of 28 GHz with isotropic element

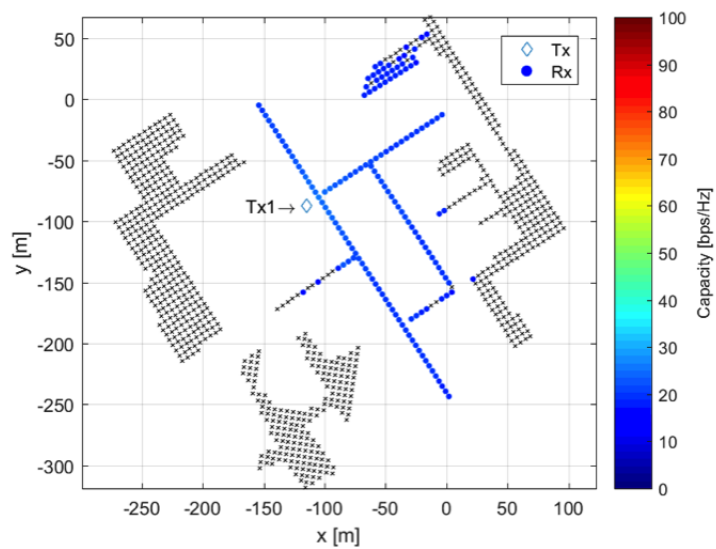


Figure A.21: Outdoor 28 GHz isotropic DET capacity

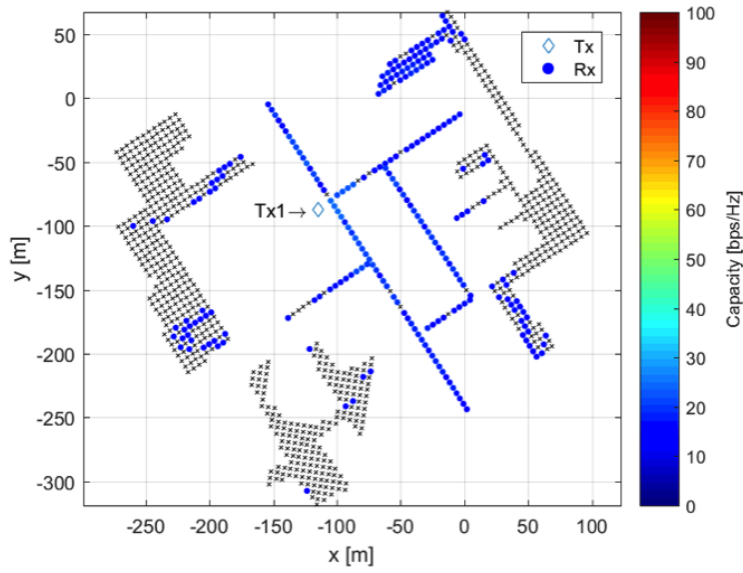


Figure A.22: Outdoor 28 GHz isotropic BF capacity

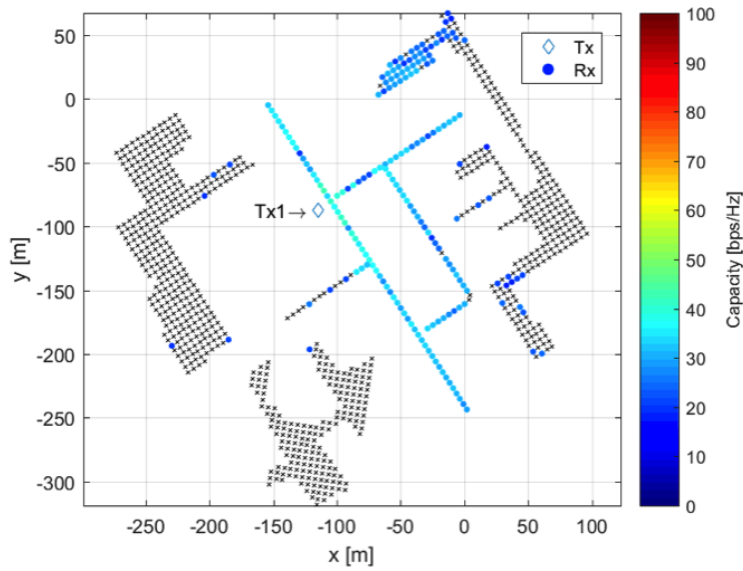


Figure A.23: Outdoor 28 GHz isotropic SMH2 capacity

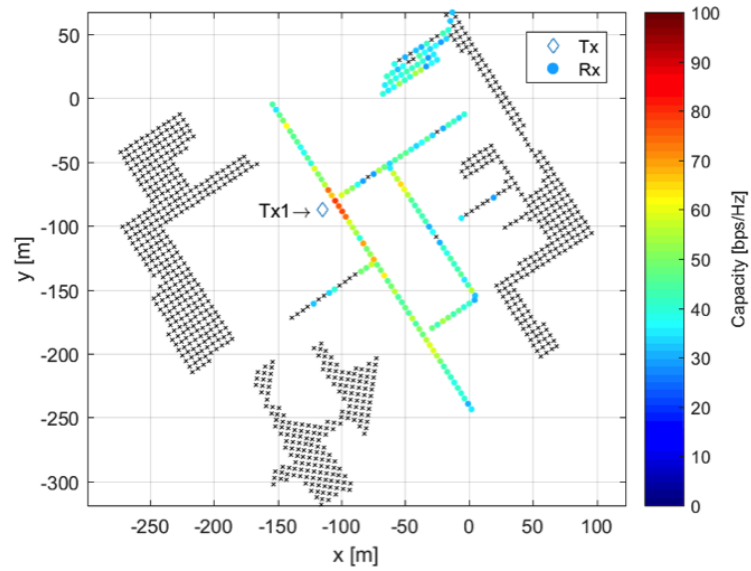


Figure A.24: Outdoor 28 GHz isotropic SMH4 capacity

#### A.2.4 Capacity of 28 GHz with patch element

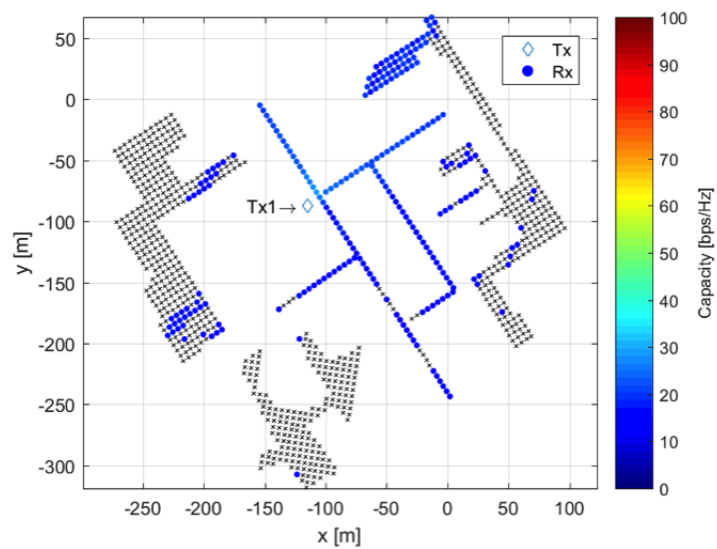


Figure A.25: Outdoor 28 GHz patch DET capacity

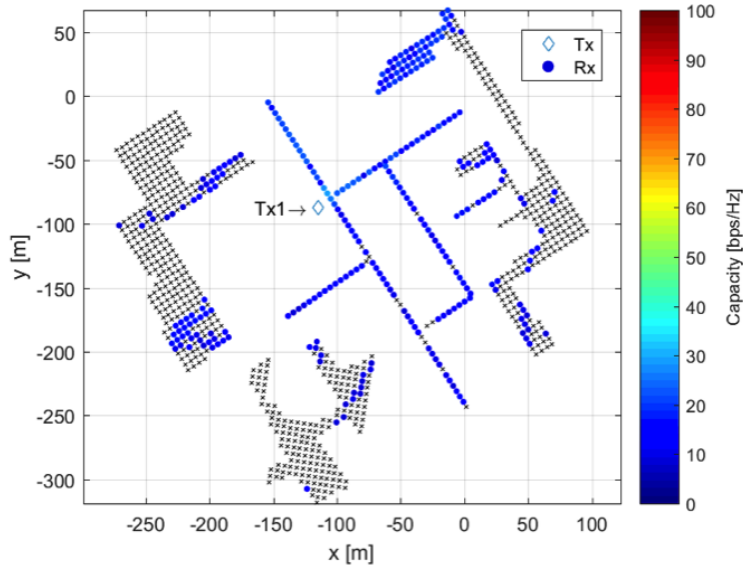


Figure A.26: Outdoor 28 GHz patch BF capacity

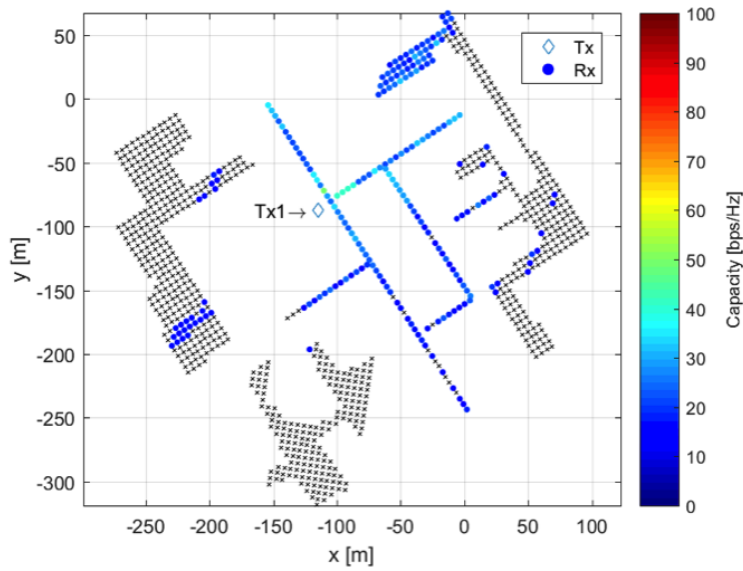
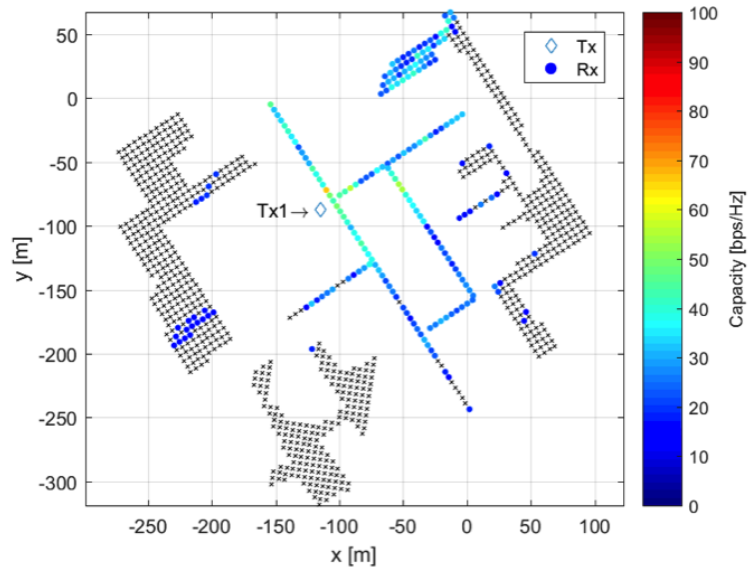


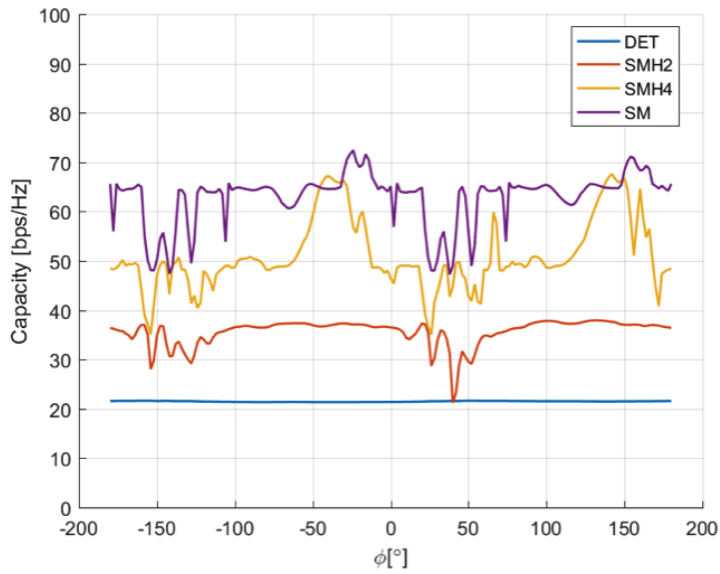
Figure A.27: Outdoor 28 GHz patch SMH2 capacity



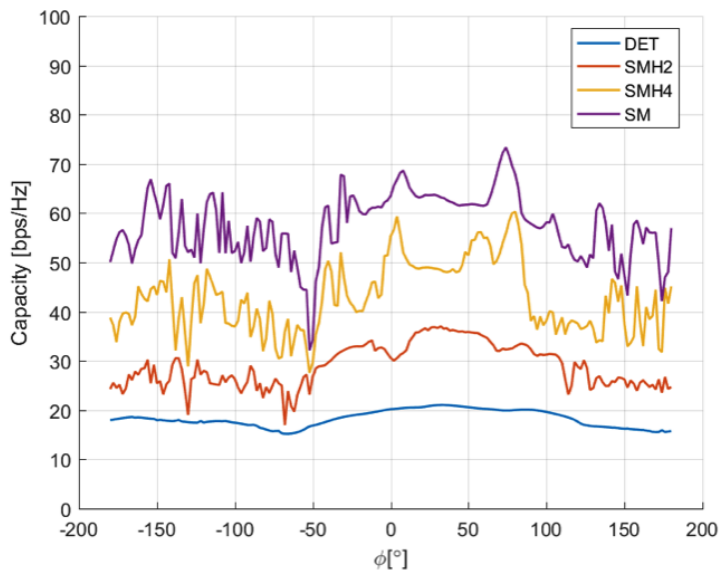


**Figure A.28:** Outdoor 28 GHz patch SMH4 capacity

### A.2.5 Capacity with rotating receivers

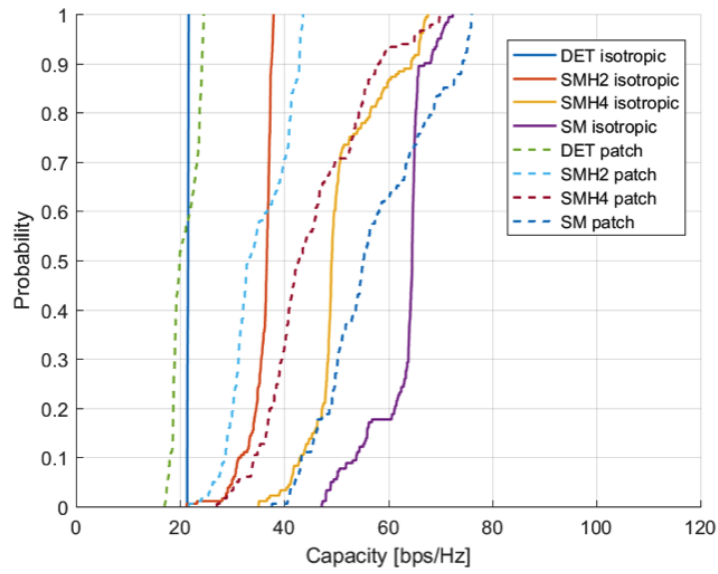


(a) Isotropic

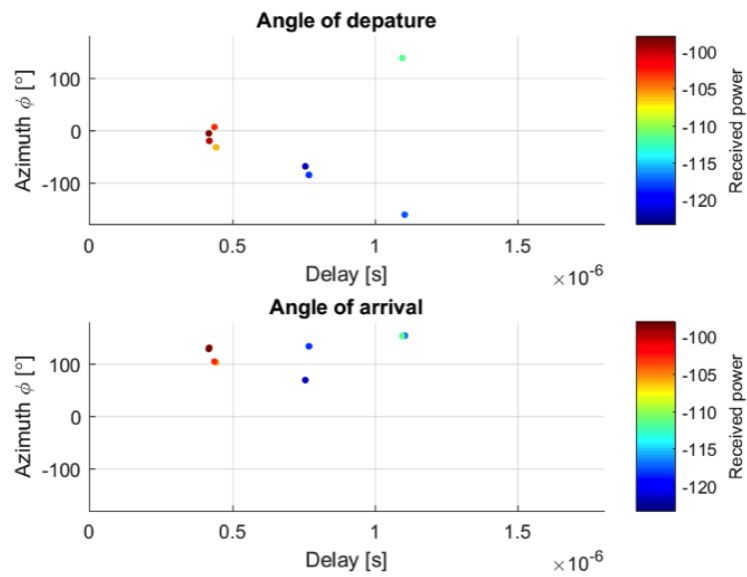


(b) Patch

**Figure A.29:** Outdoor 15 GHz rotating capacity of Rx44

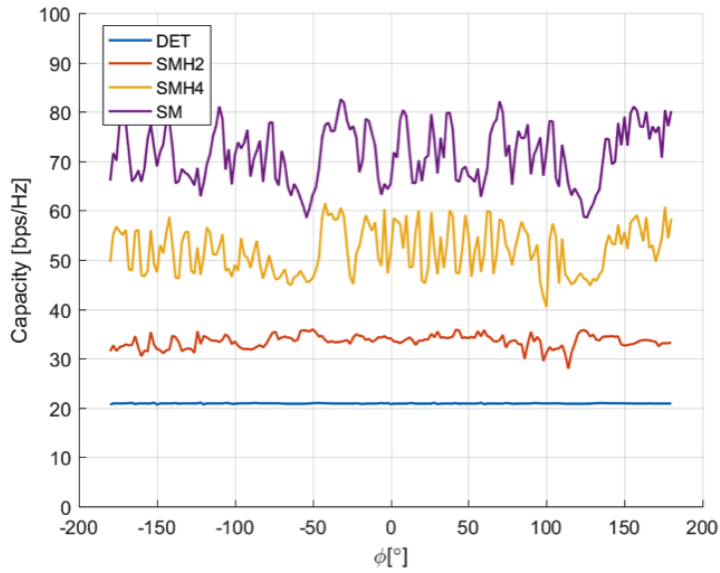


(a) Rotating capacity CDF comparison

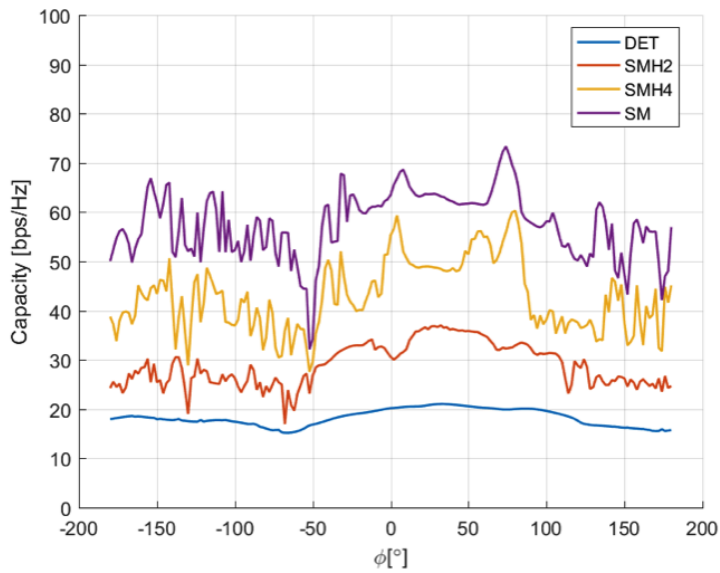


(b) AOA and AOD

Figure A.30: Outdoor 15 GHz Rx44 rotating capacity CDF and angular spread

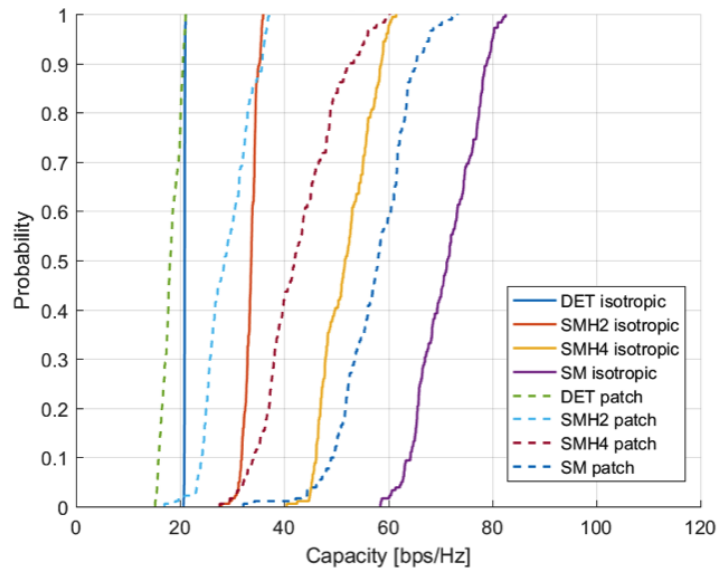


(a) 15 GHz isotropic

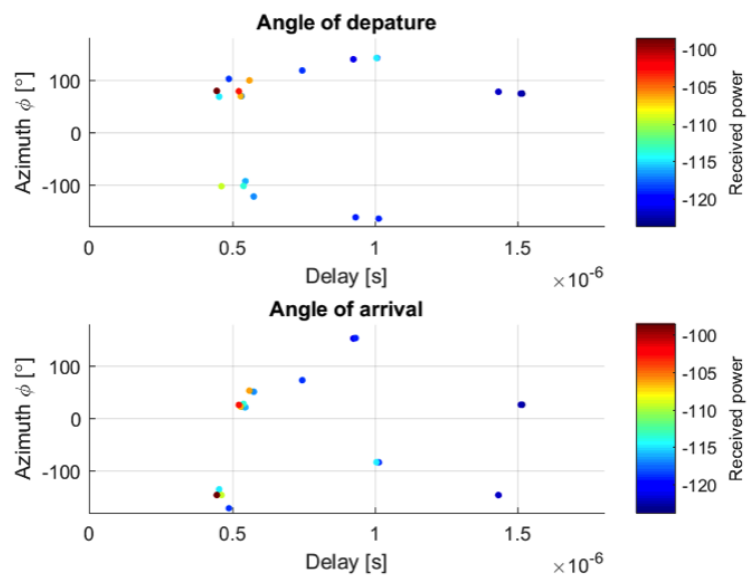


(b) 15 GHz patch

Figure A.31: Outdoor 15 GHz rotating capacity of Rx82

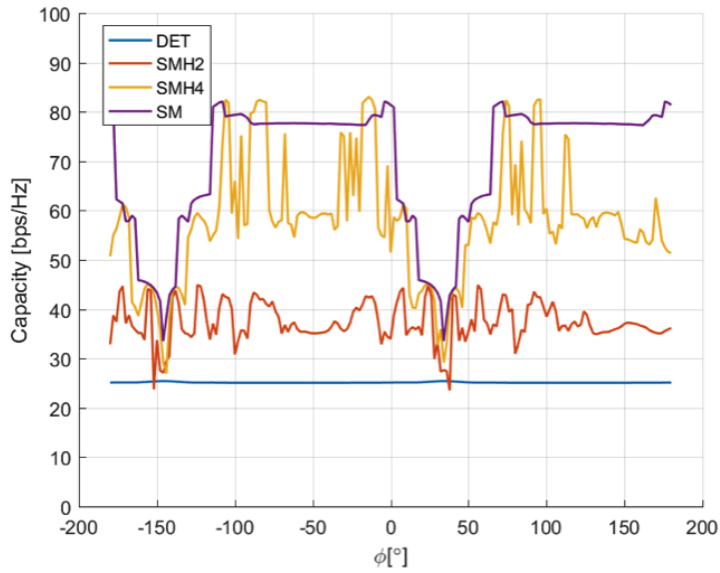


(a) Rotating capacity CDF comparison

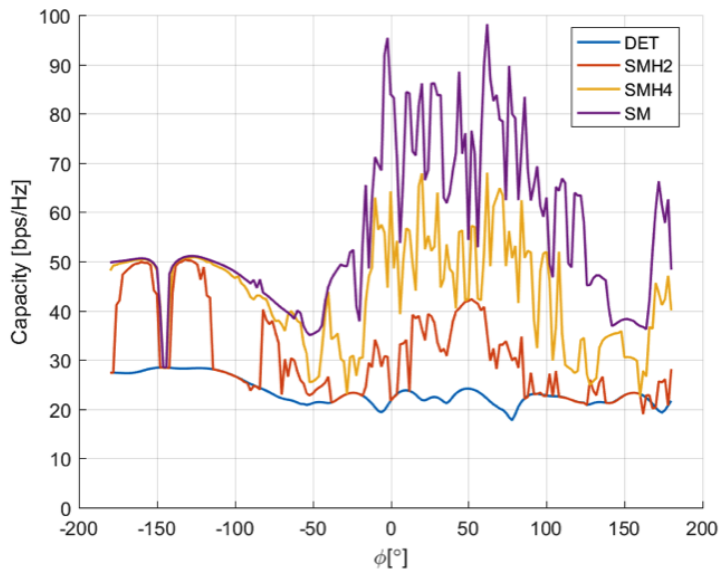


(b) AOA and AOD

Figure A.32: Outdoor 15 GHz Rx82 rotating capacity CDF and angular spread

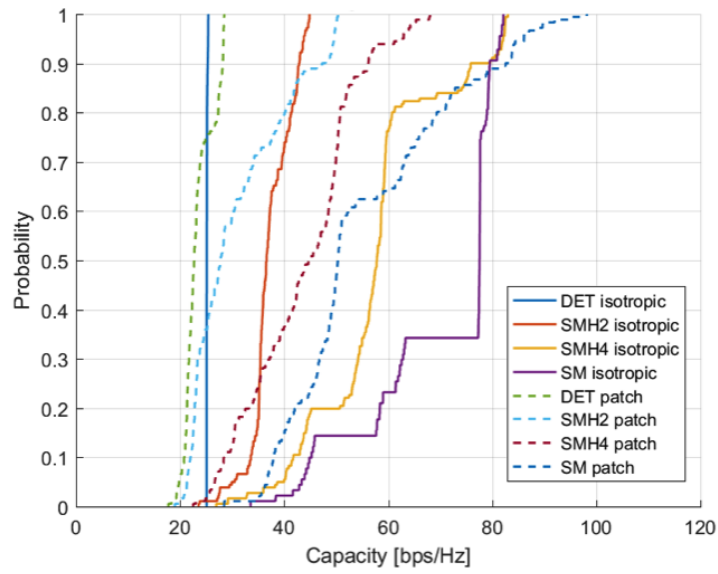


(a) Isotropic

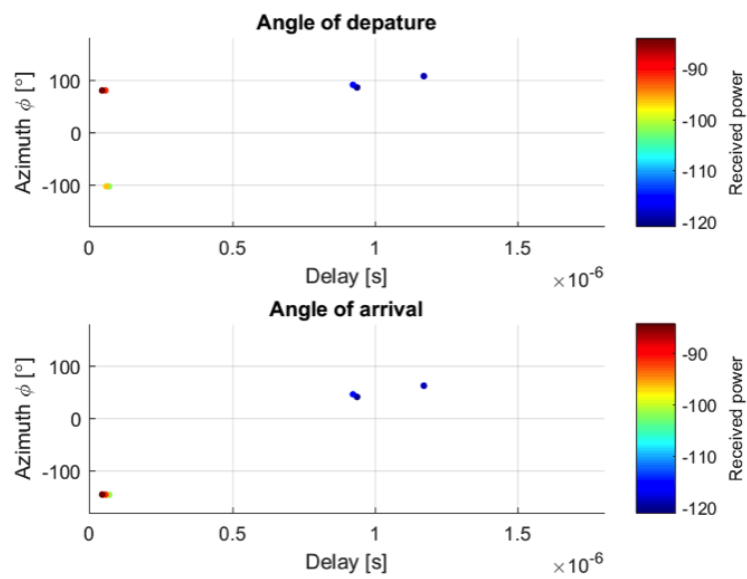


(b) Patch

Figure A.33: Outdoor 28 GHz rotating capacity of Rx19

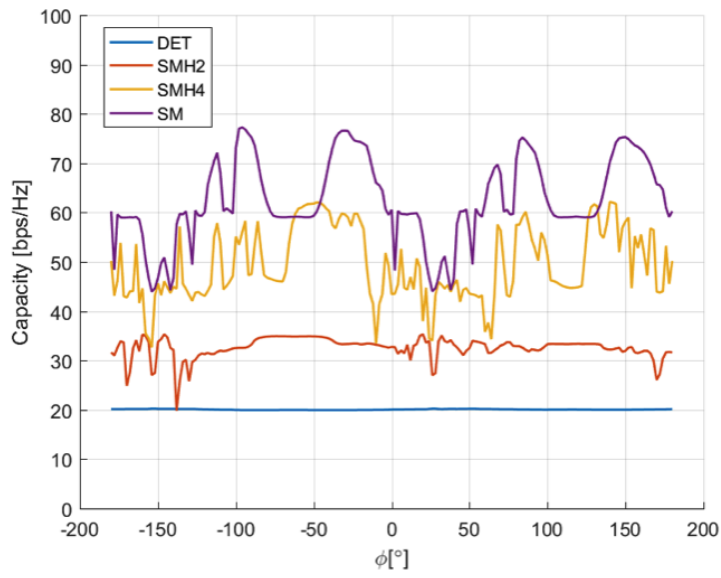


(a) Rotating capacity CDF comparison

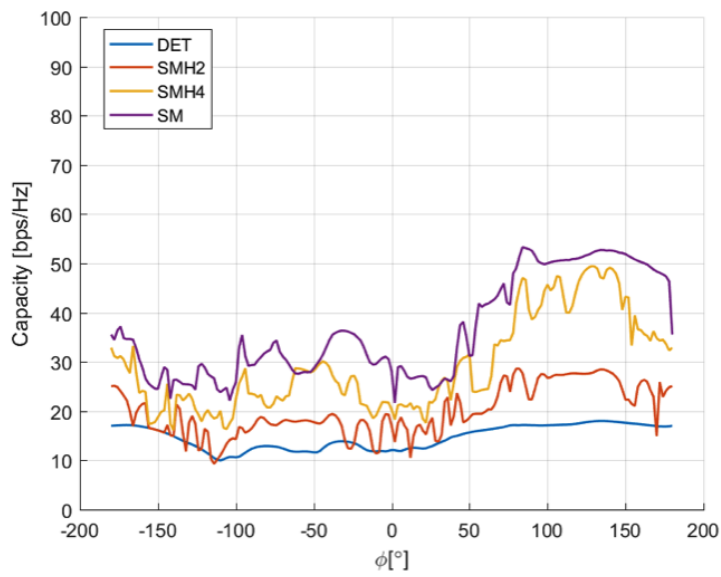


(b) AOA and AOD

Figure A.34: Outdoor 28 GHz Rx19 rotating capacity CDF and angular spread



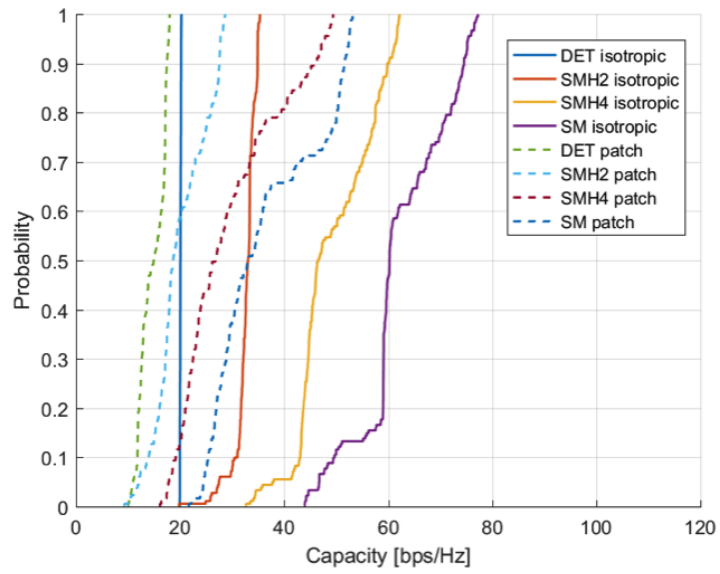
(a) Isotropic



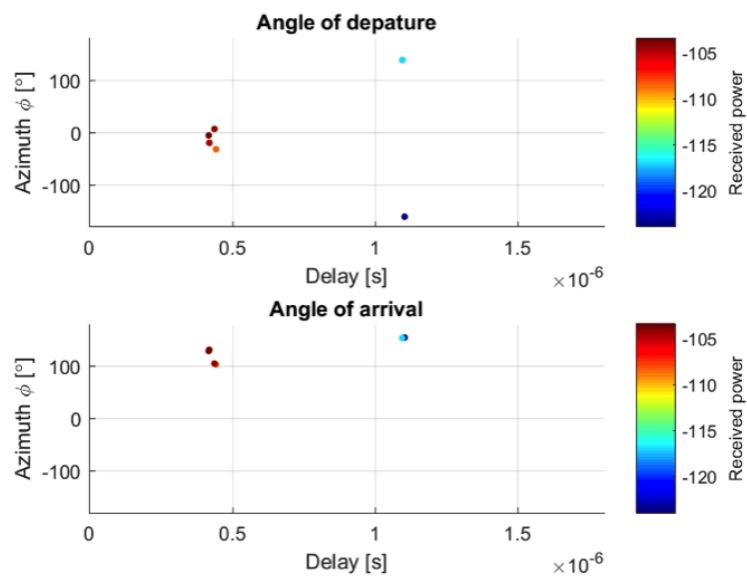
(b) Patch

Figure A.35: Outdoor 28 GHz rotating capacity of Rx44



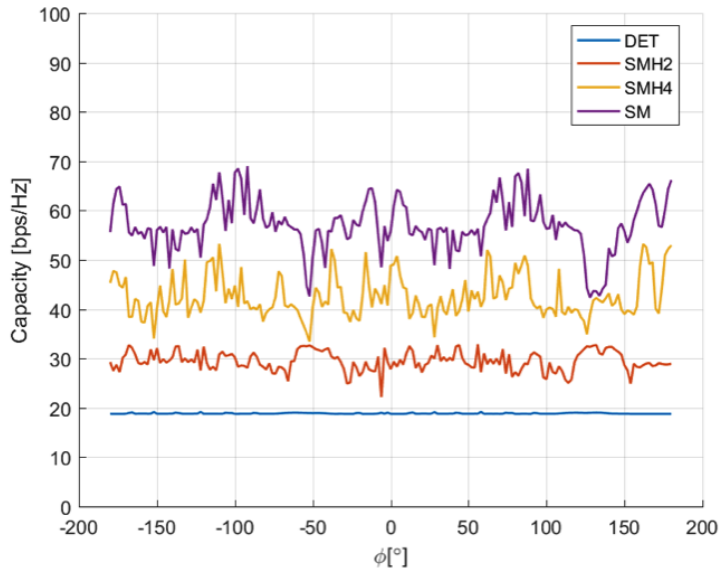


(a) Rotating capacity CDF comparison

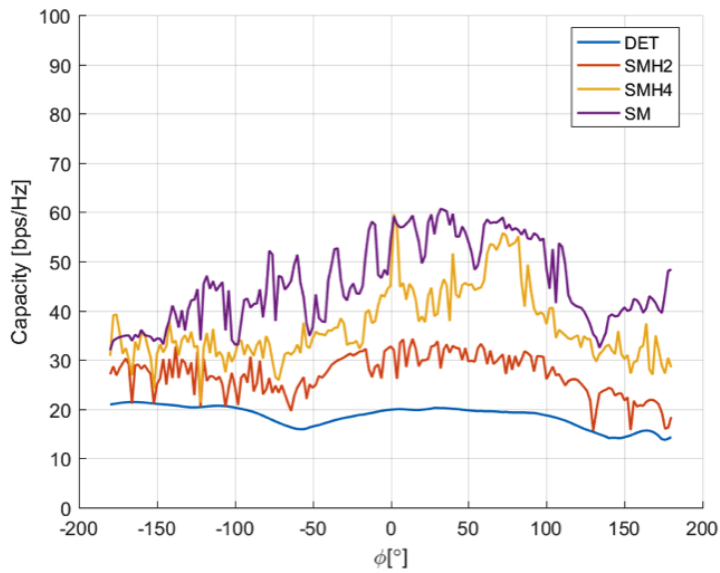


(b) AOA and AOD

Figure A.36: Outdoor 28 GHz Rx44 rotating capacity CDF and angular spread

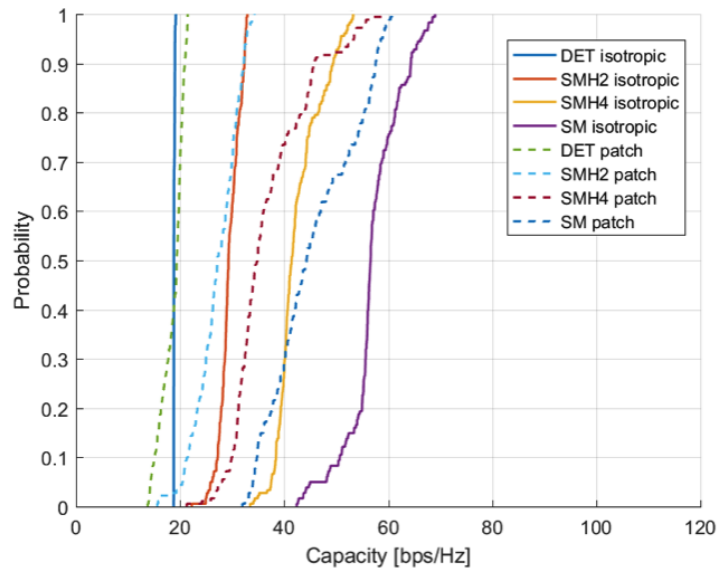


(a) 28 GHz isotropic

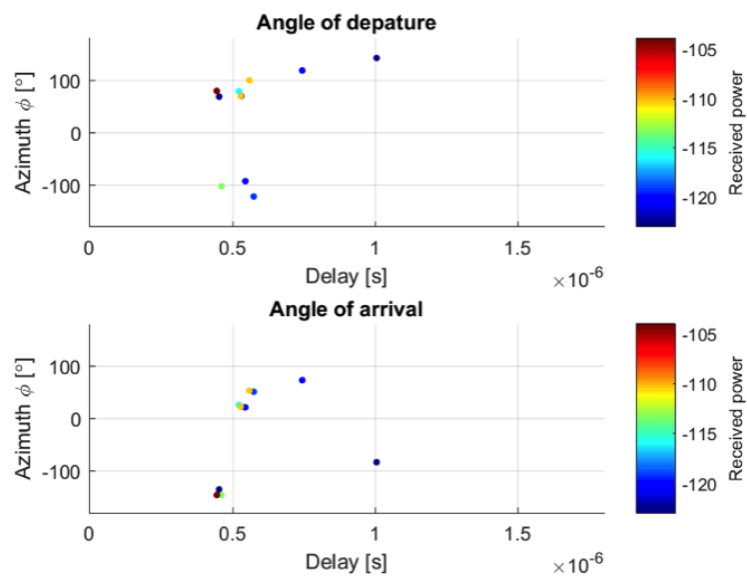


(b) 28 GHz patch

Figure A.37: Outdoor 28 GHz rotating capacity of Rx82



(a) Rotating capacity CDF comparison



(b) AOA and AOD

Figure A.38: Outdoor 28 GHz Rx82 rotating capacity CDF and angular spread